Study Of Two Phonon Octupole Vibrations in ^{146}Gd

by

Nontobeko Angel Khumalo

Dissertation submitted in partial fulfilment of the requirements for the degree of Master of Science at the University of Zululand

Supervisor: Prof. J.N. Orce

Department of Physics, University of the Western Cape

Co-supervisor: Dr. S.S. Ntshangase

Department of Physics And Engineering, University of Zululand

December, 2013

Declaration

I, the undersigned, hereby declare that the work contained in this thesis is my own original work and that I have not previously in its entirety or in part submitted it at any university for a degree.

Signature.....

Date.....

Abstract

Recent measurements of double octupole vibrational states in ^{146}Gd have resulted in the need of deeper studies of such excitations. A state with $J^{\pi}=6^{+}$ at 3485 keV has been suggested as the two-phonon octupole excitation in ^{146}Gd. A $6^{+} \rightarrow 3^{-} \rightarrow 0^{+}$ cascade of E3 γ-ray transitions from this state supports this interpretation

This work aims at investigating this 6^{+} state and the other missing members of the octupole quartet are sought in order to accurately characterize the two-phonon octupole vibrations in nearly-spherical nuclei. The $\gamma - \gamma$ coincidence experiment, with the ^{144}Sm(α, 2n)^{146}Gd fusion-evaporation reaction at a beam energy of 26.3 MeV, was performed to produce the ^{146}Gd nucleus. The experiment was performed using the AFRODITE array at iThemba Laboratory for Acceletor-Based Sciences (LABS), South Africa. Eight clover detectors were used, with four at 90° and four at 135°, and they were surrounded by the BGO shields for compton suppression. With the highly efficient AFRODITE array, the experiment provided good quality data which was sorted into $\gamma - \gamma$ matrices. From these matrices, the total projection spectrum was obtained. A gate on a 382 keV γ-ray transition was made to see if the suggested 1905 keV γ-ray transition from the $J^{\pi} = 6^{+}$ state to the $J^{\pi} = 3^{-}$ state will be observed. From the 382 keV gated spectrum, there was no evidence of the 1905 keV γ-ray transition. The branching ratios of the 826 and 502 keV transitions were measured and the limit to the intensity of the 1905 keV peak has been set. The limit was set to $\leq$6 intensity for the unobserved 1905 keV γ-ray transition . Our work show no evidence of the 1905 keV γ-ray transition and thus no octupole vibrations in ^{146}Gd. However, limitations in the sensitivity of our experiment may leave an open door to further investigate the existence of the two-phonon octupole excitation in ^{146}Gd nucleus.

Dedication

- To my parents Mr J.B. Khumalo and Mrs S.G. Khumalo (KaMadela).

-To my brother Msawenkosi and my sisters Lungile, Anele, Asamkele and Phumla.

-To my grandmother Mrs T. Madela (MaMbatha).

Acknowledgements

"It does not, therefore, depend on man's desire or effort, but on God's mercy" - Romans 9:16

First and foremost, I would like to thank God for giving me strength and sustaining me throughout this work. It is His loving kindness and mercy that has brought me this far.

I would like to express my gratitude to my supervisor, Prof. J.N. Orce, for all the support he gave me. ¡muchas gracias.

I thank my co-supervisor, Dr. S.S. Ntshangase, for his assistance in administration processes at the university, for his support and words of encouragement to work hard and finish this work.

I want to thank Prof. O.M Ndwandwe for giving me the opportunity to join the Manus/-Matsci program.

I thank iThemba LABS for the beam time and the equipment used for this research work, Mrs N.Y. Kheswa for preparing the target and her help in understanding the preparation of the target and the AFRODITE group for taking shifts.

I thank all the post graduate students at iThemba LABS for their support and the fruitful interactions I had with them. Not forgeting the senior researchers whom I knocked on their doors.

Many thanks to Dr. P. Jones for his help with the digital system, from the system set up to data sorting. I would also like to thank Siyabonga Majola and Vincent Kheswa for spending their nights at the lab working on the digital system set up, and thank you Siya for taking your time to read my thesis.

My special thanks goes to Dr. T.S. Dinoko for his endless help in this work. I thank you for your help with data sorting, analysis and latex. Thanks for being patient with me and all the questions I asked you, you were always a shout away. The words of encouragement you gave me always made this research life a bit more bearable. Ke a leboga ntate! Modimo a go segofatse.

I would love to thank Prof. B. Rubio and Prof. S. Yates for taking their time to look at my data. Thanks Steve for proofreading my thesis, your input was highly appreciated.

I thank Mr T. Jili for taking your time, in such short notice, to read my thesis.

I thank the National Research Foundation and SANHARP for funding through the Manus/-Matsci program. I wouldn't have done this work in an empty stomach.

I want to thank my cousin, Nomusa Mpanza. You were there since the first day of my university studies and you have been there for all these years of studying. Ngiyabonga Mthiya, uNkulunkulu akubusise, wena nomndeni wakho.

I would like to extend my heartfelt gratitude to my aunt, Nonhlahla Mkhwanazi, for her contribution to my studies. I thank the whole family for all the assistance and support you gave me. You have been supportive since the beginning. Ngiyabonga boShamase. Amanda, thank you for all the little chats we had, they always kept me inspired and motivated.

How can I forget my partners in crime! I want to thank my best friends; Nana Thabezhe, C.T Thethwayo and Phumlani Sithole for their love and support, they always had my back. You guys are the best!

Lastly, but by no means the least, I want to thank my family, the people who have kept me going through all these years. I thank my siblings for bearing with me, I owe you guys! My parents for supporting me even though they had no idea of what I was doing. Ngiyabonga bazali bami ngothando nangokungeseka kwenu kulo msebenzi. Kakhulu ngibonga imikhuleko yenu, yiyo engenze ngaze ngafika la. Ngiyabonga Mntungwa nawe Lingode. Sekuseduze phambili, kungekudala nizobe senidla izinyoni zabantwana benu. UNkulunkulu aze angigcinele nina.

Contents

List of Tables

List of Figures

Chapter 1

Introduction

Studies of nuclear vibrations have been performed for many years and have focused on quadrupole vibrations and not octupole vibrations. Octupole vibrations are, however, much more complex than the other modes of vibrations, such as dipole and quadrupole, and little is known about them. So far, there are only two known even-even nuclei that have first excited state of 3^-, ^{146}Gd and ^{208}Pb, and it is for this reason that searches for two-phonon octupole vibrations have concentrated on these nuclei. In ^{146}Gd, the octupole phonon lies 1 MeV lower than in ^{208}Pb [1]. That is, the octupole degree of freedom may easily get excited and observed. Most previous studies were focusing on the ^{208}Pb nucleus, and it is only recently that this search for the octupole vibrations in spherical nuclei has expanded to the ^{146}Gd nucleus.

This research project is aimed at searching for the octupole vibrations in ^{146}Gd, specifically, to identify the members of the two-phonon octupole quartet in this nucleus. In an in-beam experiment, a $6^+ \rightarrow 3^- \rightarrow 0^+$ cascade of E3 γ-ray transition was observed, hence a $J^\pi=6^+$ state at 3485 keV was suggested [2, 3]. We performed an experiment to reinvestigate these findings with a better experimental set up at iThemba Laboratory Acceletor-Based Sciences (LABS).

In this work, a similar experiment to the previous work, done by Caballero *et al* [2], was performed. The same ^{144}Sm(α, 2n) fusion-evaporation reaction, using the ^{144}Sm target of similar thickness (3.0 mg/cm^2) and the α particles at about same beam energy of 26.3 MeV. A difference was that the target used in the present work was enriched to 85.91 % while the target used in the previous measurements was enriched to 97.6 %. In our experiment, we used the AFRODITE array[3] at iThemba LABS which consisted of 8 high purity Germanium (HPGe) clover detectors surrounded with bismuth germanate (BGO) shields. The AFRODITE array was equipped with four clover detectors at 90° and the other four at 135°. The previous experiment [2] was performed at the Institute for Nuclear Physics of the University of Cologne, Germany. They had a compact array of nine individual Ge detectors placed at 90°, ±45° and ±35° to the beam direction but only five of them had anti-Compton shields. They also had a high-efficient EUROBALL CLUSTER detector placed at 90° to act as a non-orthogonal γ-ray polarimeter [2]. The clover detectors of the AFRODITE array were all surrounded by BGO shields for Compton supression and, therefore, it was expected to provide better quality data with less background and contaminants. The experimental results are given in Chapter 4 and are discussed in the last chapter.

The next chapter contains detail discussion of the liquid drop model, the shell model and the collective model. It then looks at magic numbers and, lastly, collective nuclear motions, i.e., nuclear vibrations and rotations. In Chapter 3 we discuss the experimental techniques, the equipment used and the procedures of the experiment. Chapter 4 explains the methods used in data analysis and shows the experimental results. Chapter 5, which is the final chapter, gives the discussion and the conclusions based on the experimental results.

[3]AFRODITE array is to be discussed in details in Section 3.4.2

Chapter 2

Literature Review

2.1 Nuclear Models

Nuclear models explain the features, composition and the behavior of a nucleus. The nucleus is now understood as quantum system composed of protons and neutrons, called nucleons, and to explain the interactions between these nucleons one has to use nuclear models. Among these nuclear models are the liquid drop model, shell model and the collective model.

2.1.1 Liquid Drop Model

The liquid drop model describes the properties of the nucleus at a macroscopic level. It was first proposed by George Gamow and was then developed by Niels Bohr [4, 5]. The model treats the nucleus as a liquid drop and uses the properties of the liquid drop to explain the properties of the nucleus and thus the name liquid drop model. It successfully explains the fission of a nucleus but it fails to describe the excited states. Figure 2.1 shows how the liquid drop model explains the nuclear fission mechanism.

This model basically assumes that a nucleus is a charged, nonpolar liquid drop held together by the strong nuclear force. The nucleus can therefore be pictured as an incompressible liquid drop.

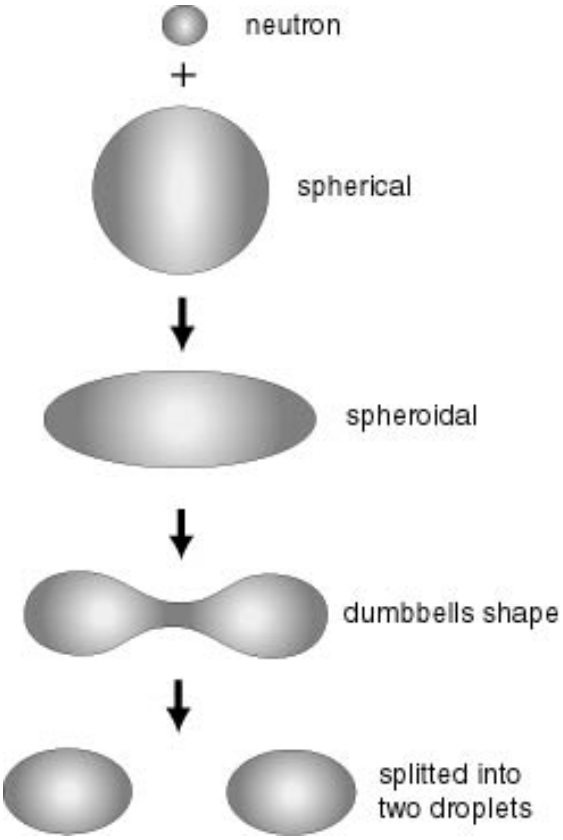

Figure 2.1: *Schematic representation of how the liquid drop model explains nuclear fission process.*

The properties of the nucleus that can be explained by this model are the binding energy, shape, size and the nucleon distribution. These nuclear properties can be described and approximated using the semi-empirical mass formula (SEMF), with the equation 2.1 [6].

$$E_B = a_V A - a_S A^{2/3} - a_C \frac{z^2}{A^{1/3}} - a_A \frac{(N-Z)^2}{A} + \delta(A,Z) \tag{2.1}$$

The SEMF shown in equation 2.1 has five terms, namely, a volume term, a surface term, the Coulomb term, the asymmetry term and the pairing term. In equation 2.1, E_B is the binding energy of the nucleus, which is affected by all the above mentioned five factors.

The volume term, $a_V A$, indicates that the binding energy depends on the volume of the nucleus, and is directly proportional to A (mass number, number of nucleons in a nucleus), because nucleons can only interact with those with which they are in contact.

The surface term, $a_S A^{2/3}$, suggests that on the surface of the nucleus there are fewer

nucleon interactions than in the interior of the nucleus, thus the binding energy is less on the surface. This is comparable to the surface tension of a liquid drop.

The Coulomb term, $a_C \frac{Z^2}{A^{1/3}}$, explains the decrease in the binding energy due to electric repulsion between protons in the nucleus. This term is also dependent on Z (atomic number), so nuclei with large atomic numbers lose more binding energy.

The asymmetry term, $a_A \frac{(N-Z)^2}{A}$, accounts for the difference in the number of protons and neutrons, if N≠Z the energy of the nucleus increases and the binding energy decreases. If N=Z, then the term will be equal to zero.

The pairing term, δ(A,Z), which is the last term, accounts for the pairing effects of the protons and neutrons. The term is negative for even A,Z, positive for odd A,Z, and zero for odd A.

These are all the factors that one can look at when describing the properties of a nucleus using the liquid drop model. However, this model only looks at a nucleus at a macroscopic level and does not explain all the properties of a nucleus. There are other properties of a nucleus that are different to those of a classic liquid drop that must be taken into account, and they cannot be explained using this model. Therefore, the shell model is needed to better describe the behaviour of a nucleus.

2.1.2 Shell Model

The shell model developed by Maria Goeppert-Mayer and Hans Jensen looks at the microscopic properties of a nucleus [7]. This model looks at the quantum nature of a nucleus and accounts for the quantal properties of the nucleus such as spins, quantum states, magnetic moments and magic numbers. In order to describe the structure of the nucleus in terms of the energy levels, this model uses Pauli Exclusion Principle; which states that two fermions may not occupy the same state at the same time [8]. Just like the liquid drop model uses a picture of a liquid drop to explain the properties of a nucleus, this model uses a picture similar to electrons in an atom. Like an electron in an atom, a nucleon in a nucleus has a set of quantum numbers that defines its state of motion. Just like electrons obey the Pauli Exclusion Principle, two nucleons cannot occupy same state at the same time. The

fact that nucleons obey the Pauli Exclusion Principle helps us to understand the relative stability of nucleon states. If two nucleons within the nucleus interact, the energy of each of them after the interaction must correspond to the energy of an unoccupied state. If these states are filled, the process simply cannot take place. In time, any given nucleon will undergo a possible interaction, but meanwhile it will have made enough revolutions in its orbit to give meaning to the notion of a nucleon state with a quantized energy.

In the atomic realm, the repetitions of physical and chemical properties that we find in the periodic table are associated with the fact that the atomic electrons arrange themselves in shells that have a special stability when fully occupied. We can take the atomic numbers of the Noble gases, 2, 10, 18, 36, 54, 86, ... as magic electron numbers that mark the completion of such shells. The nuclear realm also shows such closed shell effects that are associated with certain magic nucleon numbers: 2, 8, 20, 28, 50, 82, 126, ... A magic number is the number of nucleons (either protons or neutrons) completing a shell within the atomic nucleus. The magic numbers are, for protons, 2, 8, 20, 28, 50, 82, and, for neutrons, 2, 8, 20, 28, 50, 82, 126. Figure 2.2 is the nuclear chart which shows different regions of nuclei and the region of stable nuclei is indicated by the black squares.

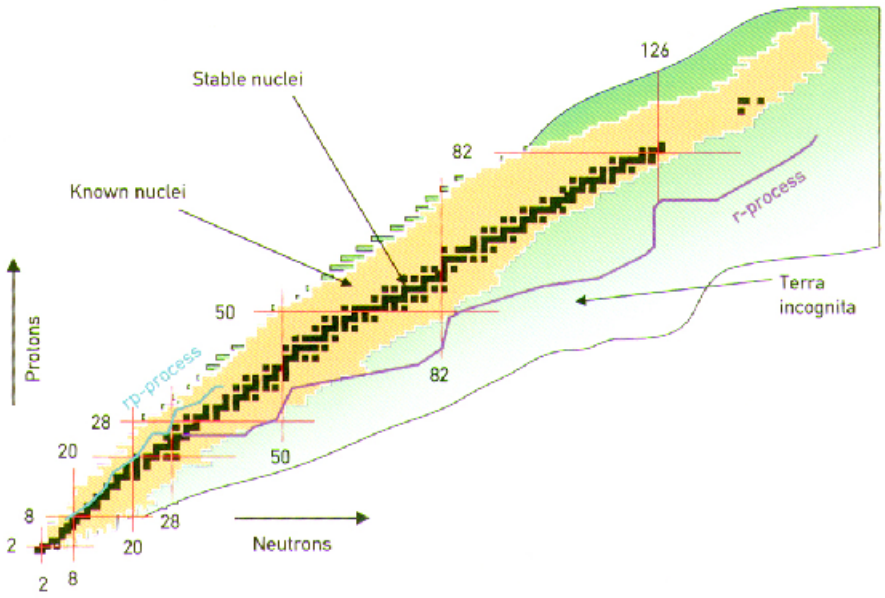

Figure 2.2: *Chart of nuclei with magic numbers indicated by red solid lines and region of stable nuclei indicated by black dots [10].*

Nuclei with a neutron or proton number equal to a magic number have a higher average

binding energy per nucleon and, therefore, are more stable. Some nuclides have both their neutron and proton number as magic numbers and are called doubly closed shell nuclei. Examples of such nuclei are, ^{4}He, ^{16}O, ^{40}Ca, etc. Figure 2.3 indicates that the shells are filled where the nucleon number is magic number. Even-even nuclei (even number of protons and even number of neutrons) exhibit these properties.

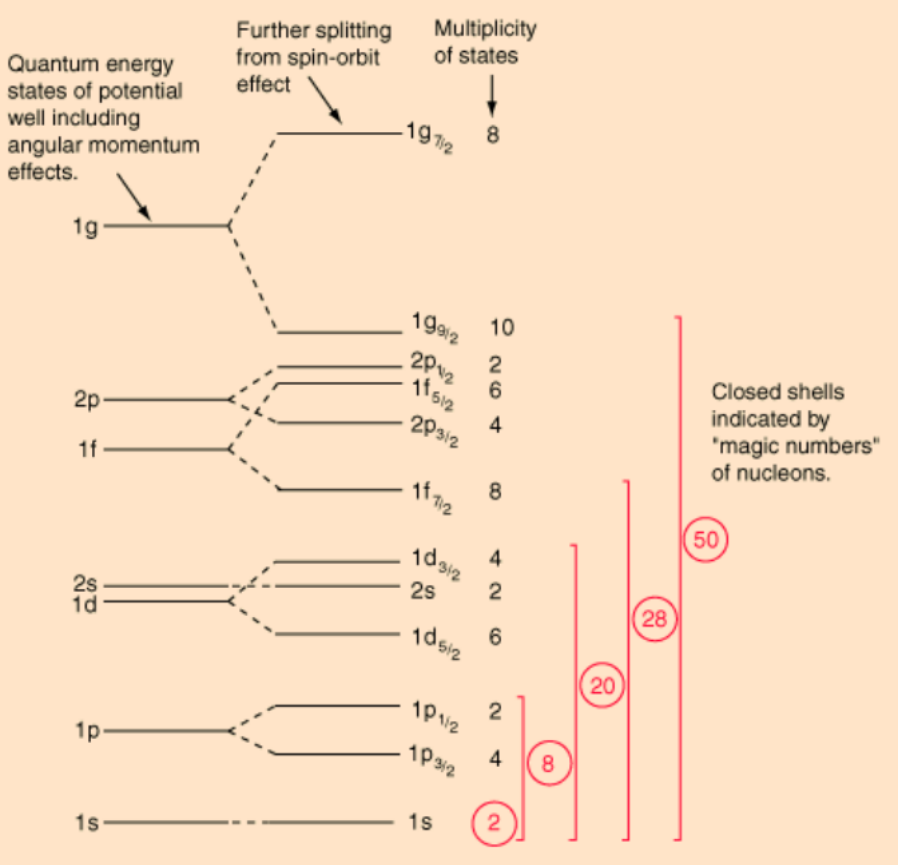

Figure 2.3: *Schematic representation of energy levels in the nuclear shell model; the shells are filled where the nucleon number is magic number [11].*

Any nucleus whose proton number or neutron number has one of these values "magic numbers" turns out to have a special stability that may be made in a variety of ways. For example, an alpha particle is exceptionally stable because its proton number and neutron number are both equal to 2, a magic number. An alpha particle is, therefore, said to be doubly magic because it contains filled shells of both protons and neutrons. The central idea of a closed shell is that a single particle outside a closed shell can be relatively easily removed but that considerably more energy must be expended to remove a particle from

the shell itself. There is much additional experimental evidence that the nucleons in a nucleus form closed shells and that these shells exhibit stable properties [9].

Wave mechanics can account beautifully for the magic electron numbers, that is, for the population of the orbitals into which atomic electrons are grouped. It turns out that, by making certain reasonable assumptions, wave mechanics can account equally well for the magic nucleon numbers. The shell model could not properly describe the properties of the nucleus, as a result the collective model was developed.

2.1.3 Collective Model

The collective model was developed by Aage Bohr and Ben Mottelson [**?**]. It combines the concepts of the liquid drop model and the shell model into a single model that describes both the macroscopic and microscopic aspects of nuclear matter in a single comprehensive framework; it views a nucleus as a collective body. This model uses the motion of the nucleons outside the closed shell combined with the motion of the paired nucleons in the core to explain the high energy states of the nucleus and certain magnetic and electric properties of the nucleus. It includes the motion of the whole nucleus such as rotations and vibrations.

2.2 Collective Nuclear Motions

Collective motions are due to the interactions between valence and core nucleons of the nucleus and are related to the liquid drop model. There are two major types of collective motions, namely, vibrations and rotations. Spherical or nearly spherical nuclei vibrate and deformed nuclei rotate and can also exhibit vibrational modes e.g. γ-vibrations, β vibrations, etc.

2.2.1 Vibrations

For the magic numbers (2, 8, 20, 28, 50, 82, 126, ...), the shape of the nucleus is generally spherical. The shape of the nucleus can be parametrized from a spherical shape corrected

by the spherical harmonics $Y_{\lambda\mu}(\theta,\phi)$. The radius vector, $R(\theta,\phi)$, can be expressed as a function of the spherical harmonics by equation 2.2.

$$R(\theta,\phi) = R_0[1 + \sum_{\lambda=0}^{\infty}\sum_{\mu=-\lambda}^{\lambda} \alpha_{\lambda\mu} Y_{\lambda\mu}(\theta,\phi)] \tag{2.2}$$

where R_0 is the radius of the spherical nucleus with the same volume, $R(\theta,\phi)$, is the distance from the centre of the nucleus to the surface at the angles (θ,ϕ) and λ is the multipole order of the shape (vibrational mode).

The three lowest vibrational modes of a nucleus are dipole, quadrupole and octupole and they are discussed below. Figure 2.4 shows the shapes of these vibrational modes.

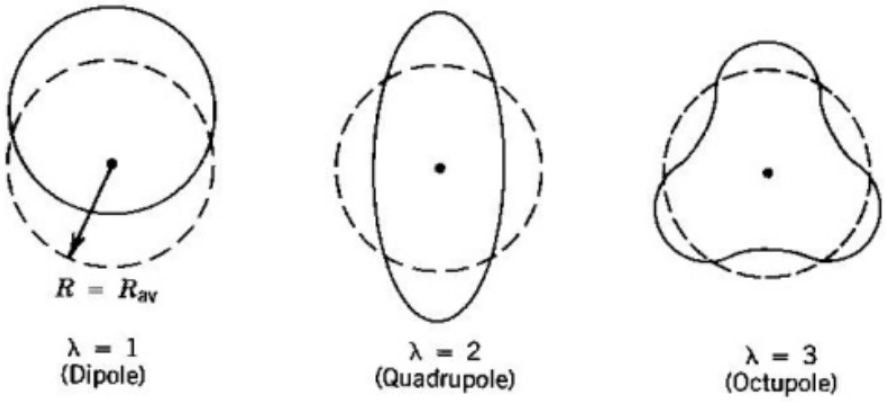

Figure 2.4: *The three lowest vibrational modes of a nucleus. The dashed line indicates the equilibrium shape and the solid line is the shape of the vibrating nucleus for each vibrational mode [13].*

Dipole $\lambda = 1$

The dipole mode corresponds to a displacement of the centre of mass and, therefore, cannot be a result of internal nuclear forces, but it results from vibrations of the nuclear surface [?]. Figure 2.4 shows the displacement in structure due to the fact that the protons and neutrons are oscillating in phase. The dipole vibrational mode has no effect on nucleus shape, as shown in Figure 2.4.

Quadrupole $\lambda = 2$

Figure 2.4 shows the shape of a quadrupole vibrating nucleus. The quadrupole mode is the most important collective low energy excitations of the nucleus. Collective vibrational modes can accept energy only in discrete amounts and these quanta of energy are called phonons. Phonons represent excited states in quantization of the modes of vibrations of elastic structure of interacting particles, and like photons of electromagnetic energy, they obey Bose-Einstein statistics. A phonon is a vibrational quantum and, therefore, a quadrupole vibrational quantum is called a quadrupole phonon. The quadrupole phonon carries two units of angular momentum (units $\hbar$), i.e., $J^{\pi}=2^{+}$.

The ground state is the phonon vacuum $\mid N = 0, \lambda=0\rangle$ and its energy is the zero point energy, where N is the phonon number. The first excited state is the multiplet (one phonon state) with angular momentum J = 2, i.e., a 2^{+} state, $\mid N = 1, \lambda=2\rangle$.

Using the m-scheme, in Table 2.1, it can be shown what states can be produced when coupling together two quadrupole phonon excitations of order of angular momentum J = $2\hbar$. Since phonons are bosons then identical particles can be coupled together.

Table. 2.1. *m-scheme to determine the spin and parity of the 2-quadrupole phonon states in the vibational model [14].*

J=2 m_1	J=2 m_2	M = Σ m_i	J
2	2	4	
2	1	3	
2	0	2	4
2	-1	1	
2	-2	0	
1	1	2	
1	0	1	2
1	-1	0	
0	0	0	0

In Table 2.1 only positive total M values are shown since the values are symmetric for M<0. The full set of allowed m_i values giving M$\geq$ 0 is obtained by the conditions $m_1 \geq 0$, $m_2 \leq m_1$. In even-even nuclei, adding a quadrupole phonon to the 0^{+} ground state leads

to a formation of the first excited 2^+ state. A two phonon coupling results in the three states with angular momenta: 0^+, 2^+ and 4^+, see Figure 2.5.

The three-phonon excitation results in a quintuplet of states with angular momenta 0^+, 2^+, 3^+, 4^+ and 6^+ as shown in Figure 2.5. Table 2.2 is the m-scheme table for the three quadrupole phonon states.

Table. 2.2. *m-scheme to determine the spin and parity of the 3-quadrupole phonon states in the vibrational mode. [14]*

J = 2 m_1	J = 2 m_2	J = 2 m_3	M = Σ m_i	J
2	2	2	6	
2	2	1	5	
2	2	0	4	6
2	2	-1	3	
2	2	-2	2	
2	1	1	4	
2	1	0	3	4
2	1	-1	2	
2	1	-2	1	
2	0	0	2	
2	0	-1	1	
2	0	-2	0	3
2	-1	-1	0	
1	1	1	3	
1	1	0	2	
1	1	-1	1	
1	1	-2	0	2
1	0	0	1	
1	0	-1	0	
0	0	0	0	0

The pure harmonic vibrational model predicts that the two-phonon triplet states occurs at twice the energy of the first excited 2^+ state and the three-phonon quintuplet occurs at three times the energy of the first exited 2^+ state. The nuclei that exhibit these properties are said to be harmonic vibrators and their excitation states are shown in Figure 2.5.

There are selection rules that govern the harmonic vibrational model and a nucleus has to be spherical or nearly spherical for it to exhibit vibrations. In spherical nuclei the particles

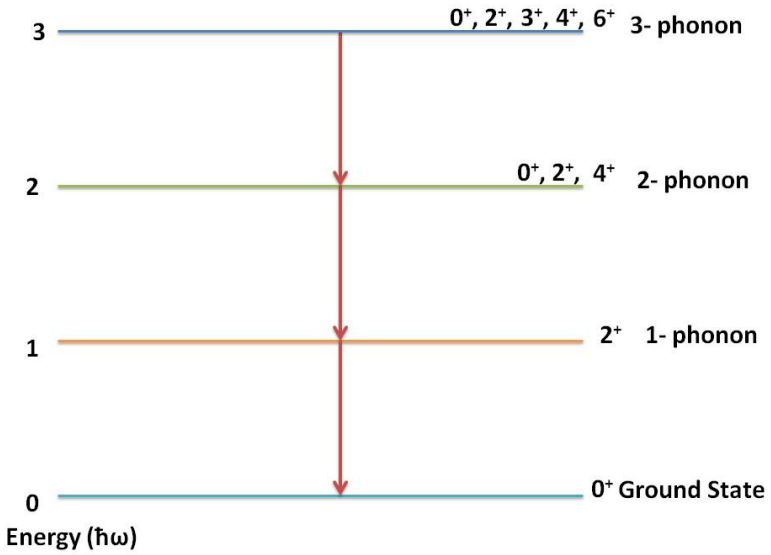

Figure 2.5: *Low-lying levels of the harmonic vibrator model showing the ground state, the single quadrupole phonon state, the two-phonon triplet, and the three-phonon quintuplet.*

are coupled to J=0 configuration. The charge distribution can characterize the shape of a nucleus, whether its deformed or spherical. The nuclear electric quadrupole moment (Q) is a parameter which describes the effective shape of the ellipsoid of nuclear charge distribution, and is given by:

$$Q = \int \rho(3Z^3 - r^2)dV \tag{2.3}$$

The above expression is the average of ($3Z^2$ - r^2) taken over the charge density distribution:

$$Q = Z(3Z^3 - r^2), with \;\; r^2 = x^2 + y^2 + z^2 \tag{2.4}$$

where Z is the total nuclear charge. A non-zero quadrupole moment (Q) indicates that the charge distribution is not spherically symmetric. For a spherical nuclei the quadrupole moment must be equal to zero (Q = 0), hence the spherical charge distribution:

$$x = y = z \Rightarrow x^2 = y^2 = z^2 \tag{2.5}$$

Substituting equation 2.5 in 2.4, $(3Z^2 - r^2) = 3Z^2 - (x^2 + y^2 + Z^2) = 0$, and therefore Q = 0. This clearly shows that for spherical nuclei Q = 0.

Below are some of the selection rules for quadrupole vibrations:

- The phonon number (N) for the electric transitions between the vibrational states can only change by one, i.e., $\Delta N = \pm 1$.
- The B(E2) values of the transitions between the 2-phonon state and the 1-phonon state should be twice the B(E2) values of the transitions between the 1-phonon state and the ground state, i.e., B(E2; N=2 $\rightarrow$ N=1) = 2B (E2; N=1 $\rightarrow$N=0).
- The B(E2) values of the transitions between the 3-phonon state and the 2-phonon state should be three times the B(E2) values of the transitions between the 1-phonon state and the ground state, i.e., B (E2; N=3 $\rightarrow$ N=2) = 3B (E2;N=1$\rightarrow$N=0).

Octupole $\lambda = 3$

The octupole vibration is the least studied mode of vibration and there is very little known about it compared to the quadrupole mode. In this vibration, a nucleus has a shape of the pear, see Figure 2.4. These vibrations come closer to the ideal harmonic oscillator as a result of the larger number of particles participating in the motion, low abundance and hence weaker mixing of negative-parity states at low excitation energies.

The nucleus that is expected to undergo octupole vibrations must have a low-lying excited state of 3^- [15]. The zero phonon state (ground state) is the zero point energy. The one phonon state is a 3^- state and the two phonon state has quartet members (0^+, 2^+, 4^+, 6^+), as shown in Figure 2.6.

The two-phonon octupole state (6^+ state) is expected to be at nearly twice the energy of the one-phonon state (3^- state). The transition between the two-phonon octupole (6^+) state and the one phonon (3^-) state and the transition between the one-phonon state (3^-) and the ground state (0^+) must be E3 transitions, i.e., there is a cascade of E3 transitions from the 6^+ state to the ground state ($6^+ \rightarrow 3^- \rightarrow 0^+$). The B(E3) value of the transition from the 6^+ state to the 3^- state should be twice that of the transition from the 3^- state

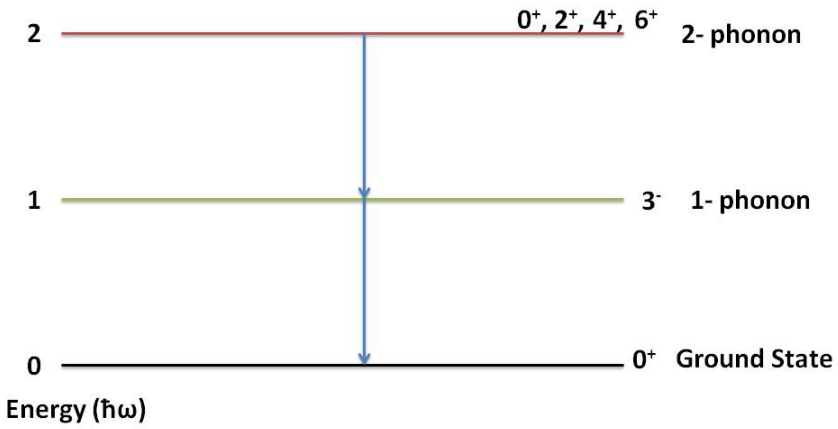

Figure 2.6: *First two phonon states of an octupole vibrating nucleus.*

to the ground state i.e., B(E3; N=2 → N=1) = 2B (E3; N=1 →N=0) [17].

2.2.2 Rotations

Nuclei are not necessarily spherical and non-spherical nuclei can rotate. A non-spherical distribution gives rise to an electric quadrupole moment, i.e.,the quadrupole moment will not be equal to zero , Q≠0. A non-zero quadrupole moment means that the nucleus is not spherical but rather deformed, and deformed nuclei exhibit rotations. The deformation of a nucleus arises from interactions of valence nucleons and thus only the valence nucleons rotates and the core is at rest.

The collective motion of nucleons about the axis perpendicular to the symetric axis produces the rotational angular momentum **R**. In addition to the rotational angular momentum, **R**, a nucleus can have the intrinsic angular momentum **J**. Therefore, the total angular momentum will then be the sum of the rotational angular momentum and the intrinsic

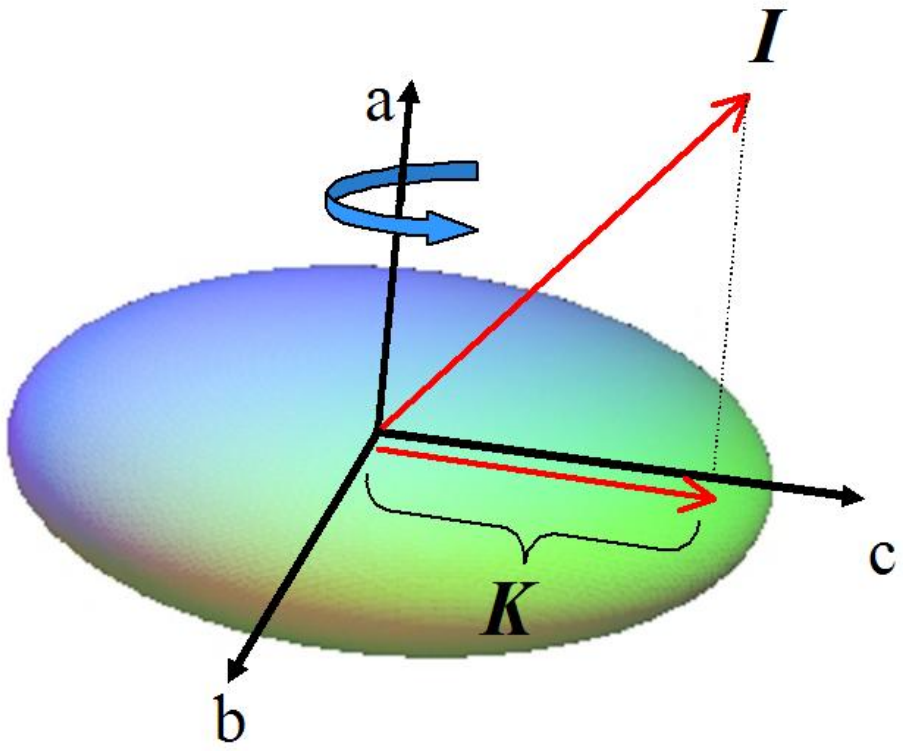

Figure 2.7: *The diagram shows a nucleus with axial symmetry showing the nuclear symmetry axis c, the rotation axis a, the total angular momentum I, and projection K onto c [18].*

angular momentum [16].

$$\mathbf{I} = \mathbf{R} + \mathbf{J} \tag{2.6}$$

The sum of the angular momentum of the individual valence nucleons gives the intrinsic angular momentum, **J**, of the valence nucleons.

$$\mathbf{J} = \sum_{i=1} \mathbf{J}_i \tag{2.7}$$

The projection of the total angular momentum, **I**, and the intrinsic angular momentum, **J**, onto the symmetry is K. For a minimum of two nucleons, the total projection K is given

by:

$$K = \sum_{i=1} \Omega_i \tag{2.8}$$

where Ω is a projection of each nucleon along the symmetry axis.

Chapter 3

Experimental Techniques And Equipment

3.1 Introduction

The atomic nucleus is a strongly interacting many-body system that exhibits a variety of shapes and excitation modes. The strong interactions between nucleons give information about the properties and the structure of a nucleus. To study the structure of a nucleus, different reactions are used, e.g. direct nucleon transfer reactions, fusion evaporation reactions, etc. Amongst these reactions, the fusion evaporation reaction will be discussed as it was used to populate the studied ^{146}Gd nucleus. The populated nucleus emits γ rays and the γ ray energies are measured through γ ray spectroscopy. This chapter discusses the γ ray interaction with matter which is important in understanding γ ray detection. It also discusses the experimental details, i.e., the techniques and the equipment used. Ultimately, the data acquisition system, which includes the digital and the analog electronics, is also discussed. This experiment was the first to be performed using the new digital data acquisition system at iThemba LABS. Therefore, the setting up and testing of the system was part of this work, hence, it is discussed in this chapter.

3.2 Gamma-Ray Interaction With Matter

In order to understand γ ray detection it is important to first understand γ ray interaction with matter. For the γ ray to be detected it must have interactions with the detector. The basic principle for the detection of any particle or radiation is that they produce charged secondary particles, which then can be collected to give an electric signal. Charged particles produce a signal within a detector by ionization and excitation of the detector material directly. However, γ rays have no charge and, therefore, cannot ionize or excite detector material. For γ rays to be detected they must have interactions in which they will transfer their energy to the electrons within the detector material. These excited electrons will then lose their energy by ionizing and exciting the atoms of the detector material. Therefore, the energy of these electrons will give information about the γ rays that they interacted with.

The γ rays interact with matter by three major processes, namely, Photoelectric Absorption, Compton Scattering and Pair Production. These processes are discussed in 3.2.1, 3.2.2 and 3.2.3.

3.2.1 Photoelectric Absorption

This process is dominant at low energy range and, therefore, is less important at higher energies. The γ ray interacts with the bound electron in an atom, it transfer its energy to the electron and the electron is ejected from its shell. Figure 3.1 shows a schematic representation of the photoelectric absorption.

Most of the γ ray energy will be transfered to the electron as its kinetic energy and some of it will be used to overcome the electron's binding energy. The ejected electron will have the kinetic energy, E_e, given by:

$$E_e = E_\gamma - E_b \tag{3.1}$$

The energy of the ejected electron is the difference between the energy of the γ ray, E_e, and the binding energy of the electron, E_b. In photoelectric absorption the γ ray transfers all

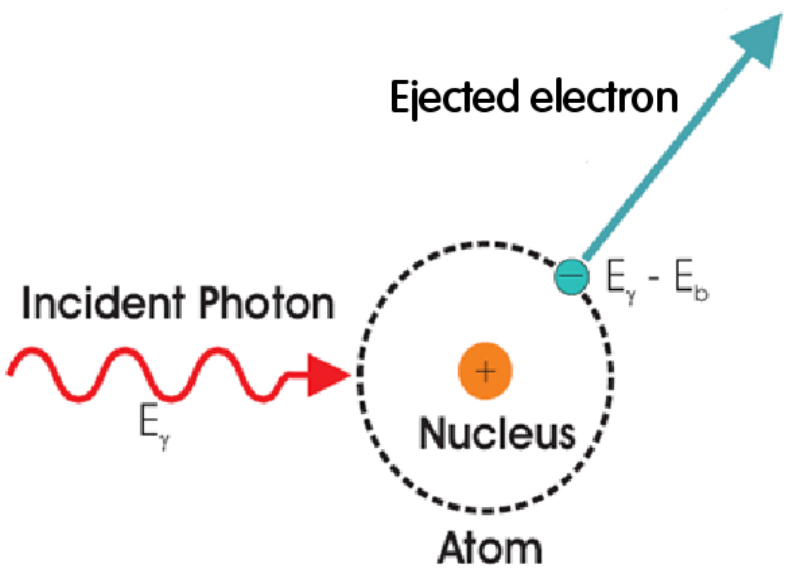

Figure 3.1: *Schematic representation of photoelectric absorption [20].*

of its energy and the resulting pulse falls in the full-energy peak and this is important for γ ray detection [21]. The energy at which an electron is ejected depends upon the energy of the γ ray. It is most likely that the electron be ejected from the K shell. If the energy is not sufficient to eject a K electron, then L or M electrons will be ejected instead. This gives rise to the discontinuities in the photoelectric absorption curves. These absorption edges occur at the binding energies corresponding to the electron shells.

The photoelectric effect occurs in two stages. First, the photon (a) (see Figure 3.2) takes out a bound electron in one atom. In the case of gamma photons, it is usually an electron belonging to the innermost layers L or K (as shown in Figure 3.2). Then the atom that has lost one of its inner electrons is left in an excited state. An electron from an outer layer (b) moves to occupy the vacancy left by the ejected electron. If the ejected electron belonged to the K shell as in the Figure 3.2, an X-ray is emitted during the transition.

The probability that a photon will undergo photoelectric absorption depends on the energy of the γ ray, binding energy of the electron and the atomic number of the atom. For the more tightly-bound electrons the probability is greater and, therefore, it is most likely that the ejected electron will be from the K shell, provided the γ ray has enough energy to overcome the binding energy of the K electron. This probability is given by equation

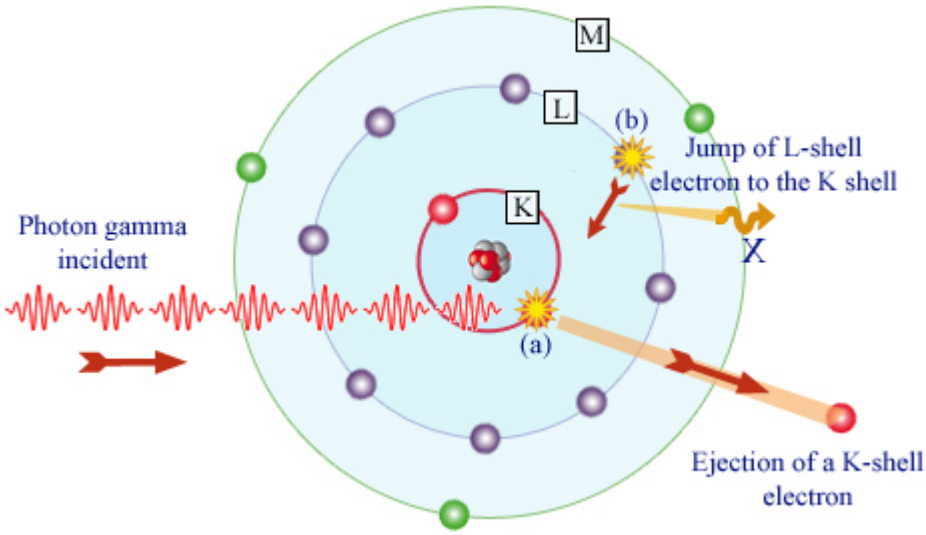

Figure 3.2: *Representation of γ absorption by an atom [22].*

3.2, which shows that the interaction is more important for heavy atoms, like lead and uranium, and low energy γ rays:

$$\tau \propto Z^4/E^3 \tag{3.2}$$

where τ = photoelectric mass attenuation coefficient. This proportionality is only approximate because the exponent of Z varies in range 4.0 to 4.8. The probability of the photoelectric absorption increases rapidly as the γ ray energy decreases (see Figure 3.3).

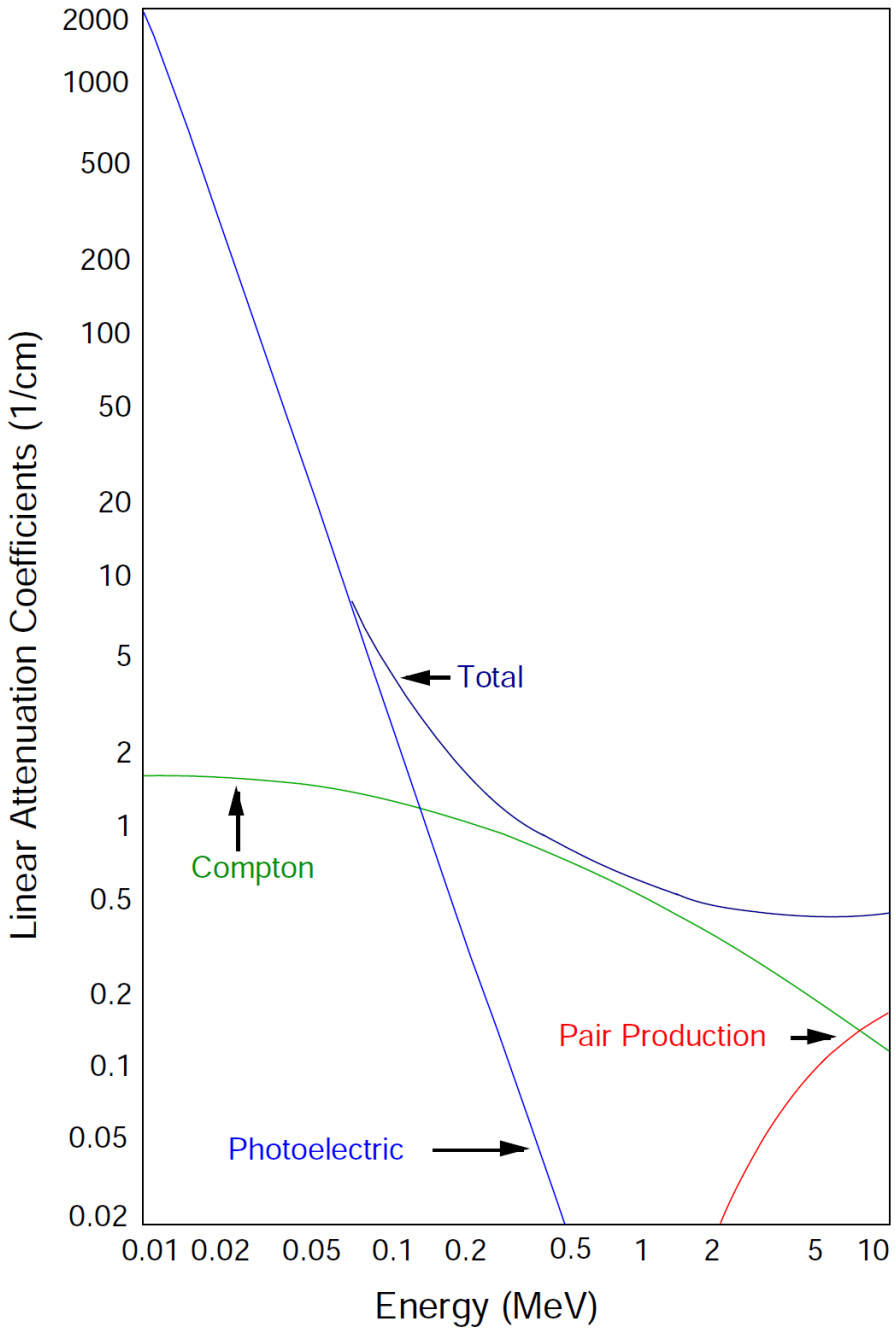

Figure 3.3: *The linear attenuation coefficient of germanium and its component parts [20].*

3.2.2 Compton Scattering

Compton scattering is the most important in the mid-energy range (100 keV to 10 MeV). The γ ray interacts directly with an electron and transfer part of its energy to the electron in one interaction (see Figure 3.4). After the interaction both particles, the γ ray and the electron, leave the interaction site. The directions these particles take depends on the amount of energy that is transfered during the interaction. The energy of the recoil electron is equal to the difference of the energy lost by the γ ray and the electron binding-energy and is given by equation 3.3.

$$E_e = E_\gamma - E' \tag{3.3}$$

where E_e is the energy of the scattered electron, E_γ is the energy of incident γ ray and E' is the energy of scattered γ ray. The kinetic energy of the electron, E_e, is nearly equal to the energy lost by the γ ray because the binding energy of the electron, E_b, is very small compared to the energy of the γ ray.

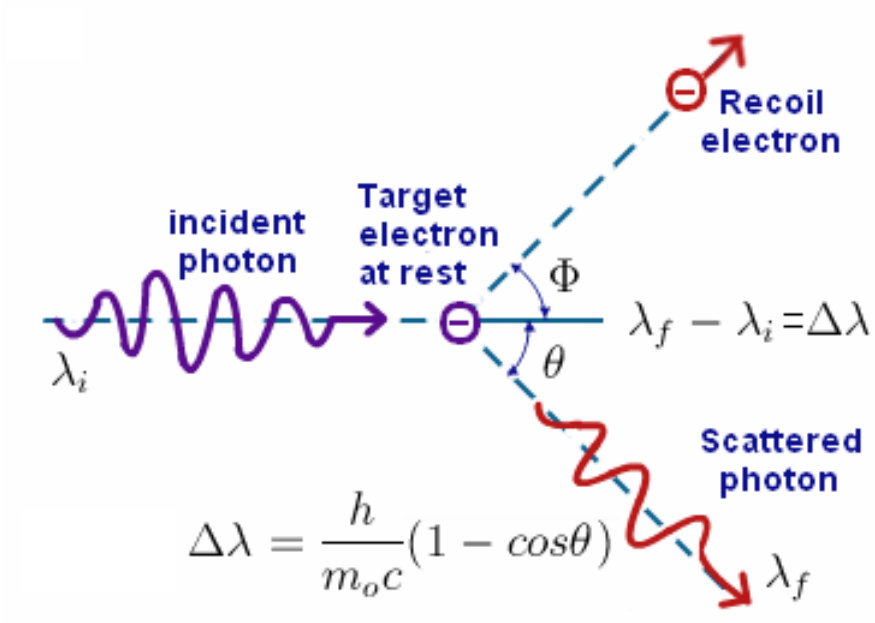

Figure 3.4: *Schematic diagram illustrating Compton Scattering [20].*

The energy of the scattered γ ray is given by equation 3.4.

$$E' = \frac{m_0c^2}{(1 - cos\theta + \frac{m_0c^2}{E})} \tag{3.4}$$

where m_0c^2 is the rest energy of the electron (511 keV) and θ is the angle between the incident and scattered photon, as shown Figure 3.4.

When Compton scattering occurs in a detector, the scattered electron is usually stopped in the detection medium and the detector produces an output pulse that is proportional to the energy lost by the incident γ ray, and that is how the energy of the γ ray can be determined. [21].

The probability of Compton scattering decreases as the energy of the γ ray increases. Figure 3.3 shows the behaviour of the three processes in which γ rays interact with matter as the energy changes. Compton scattering is weakly dependent on the atomic number of the absorbing material, Z.

3.2.3 Pair production

Pair production is dominant at high energies, as indicated in Figure 3.3. In this process the γ ray interact with the atom as a whole. By the interaction with the electric field of a nucleus, the energy of the incident photon is converted into a mass of an electron-positron pair; the γ ray transforms into an electron-positron pair. For this to happen the γ ray must have at least an energy of 1.022 MeV, which is equivalent to the combined rest mass of the two particles, with each having 0.511 MeV [6]. If the γ ray has energy greater than the combined rest mass of the electron and the positron (1.022 MeV) then the excess energy appears in the recoil of the emitting nucleus and as the kinetic energy of the pair. Figure 3.5 shows a schematic diagram of the pair production process.

The electron and the positron created in the pair production are slowed down in the detector medium and they lose their kinetic energy. The positron then combines with a free electron, the two annihilate and two annihiliation γ rays, of 0.511 MeV each, are released. The released γ rays may further interact with the detector medium or escape.

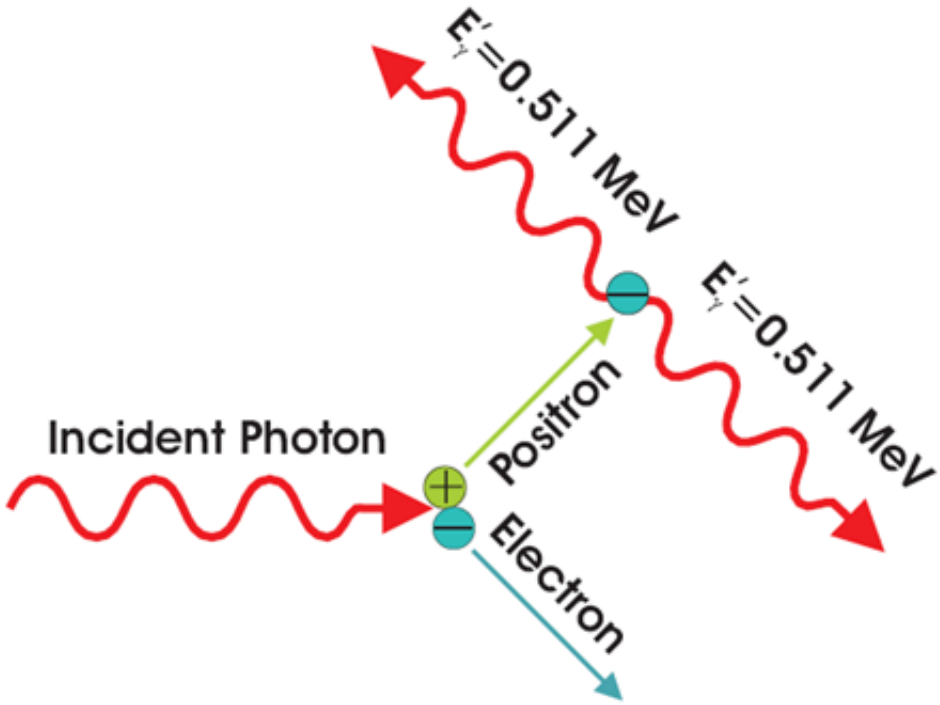

Figure 3.5: *Schematic diagram illustrating Pair Production [20].*

If both of the released annihilation γ rays are absorbed in the detector, the interaction will contribute to the full-energy peak; if only one of the annihilation γ rays is absorbed in the detector, i.e. the other escapes, the interaction contributes to the single-escape peak at 0.511 MeV. If both annihilation γ rays escape, the interaction contributes to the double-escape peak at 1.022 MeV below the full energy peak. The relative heights of the three peaks depend on the energy of the incident γ ray and the size of the detector. The probability of Pair Production process to occur increases as the energy of the γ ray increases, see Figure 3.3 [20].

3.3 Fusion Evaporation Reaction

^{146}Gd is an unstable nucleus, with the half life of 48.3 days. It is not a naturally occuring isotope, but it is only two protons away from the stable ^{144}Sm nucleus. A fusion evaporation reaction is the most suitable way to produce the ^{146}Gd nucleus and to populate the non-yrast states which will be investigated in this work.

When an experiment is conducted with this kind of reaction (the fusion evaporation reaction), a target nucleus is bombarded with a projectile nucleus to produce a compound nucleus, as illustrated in Figure 3.6. The projectile nucleus, incident on a target, must have enough kinetic energy to overcome the Coulomb barrier, V_{CB} (see equation 3.5), between the projectile and the target nucleus [23].

$$V_{CB} = \frac{1}{4\pi\varepsilon_0}\left(\frac{Z_p Z_t e^2}{R}\right) \tag{3.5}$$

where Z_p is the atomic number of the projectile nucleus, Z_t is the atomic number of the target nucleus, ε_0 is the permittivity of free space, e is the charge of the electron and R is the distance between the projectile and the target nuclei. [24].

The compound nucleus is formed in an excited state. Its excitation energy E_x, given by equation 3.6, depends on the centre of mass, kinetic energy of the collision and the Q-value of the reaction.

$$E_x = Q + E_b\left(1 - \frac{A_b}{A_p + A_t}\right) \tag{3.6}$$

where E_b is the beam energy in the laboratory reference frame, A_p is the mass number of the projectile nucleus and A_t is the mass number of the target nucleus. Q, in equation 3.6, is the Q-value of the reaction and is given by equation 3.7.

$$Q = \sum m_i - \sum m_f = A_p + A_t - m_{CN} \tag{3.7}$$

m_i and m_f are the masses of initial and final states [25]. The excited compound nucleus could lose its energy by evaporating neutrons or protons and if it has enough energy it can emit alpha particles. After particle emission, a nucleus deexcite to its ground state by emitting γ rays.

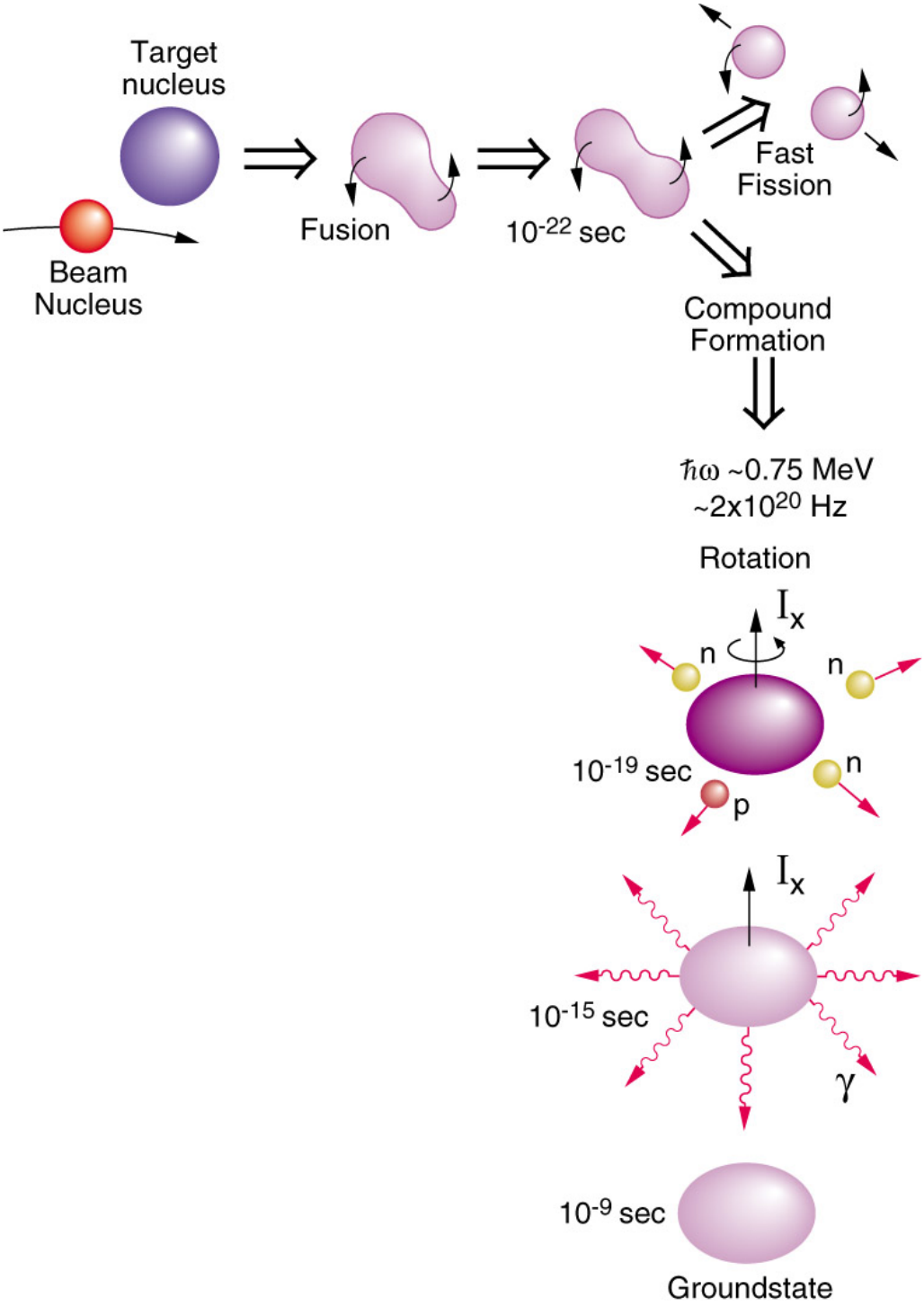

Figure 3.6: *Schematic representation of fusion evaporation reaction [12].*

3.4 The Experiment

To study the behaviour of a nucleus in an excited state, sophisticated spectroscopic instruments and techniques are used. At iThemba LABS the AFRODITE array of HPGe clover detectors is used for γ ray detection and gives information about the nucleus in an excited state. This section explains in detail the procedures of the experiment and the equipment used.

3.4.1 Target Preparation

As mentioned earlier, ^{146}Gd is an unstable nucleus and, therefore, one needs to produce it. The most suitable reaction to produce the nucleus, ^{146}Gd, is through the fusion evaporation reaction using ^{144}Sm as a target nucleus. Below the ^{144}Sm target preparation process is outlined.

Targets were supplied by the iThemba LABS dedicated target laboratory and manufactured by Mrs N.Y. Kheswa *et al.* The isotopic enrichment of the material was 85.91% and it was obtained from an external supplier. The manufacturing process of targets involved melting the ^{144}Sm powder under vacuum by electron heating with the electron-gun. This was followed by mechanical rolling of the melted metal under an argon atmosphere to prevent oxidation. Two targets were manufactured and their thicknesses after rolling were measured by X-ray fluorescence (XRF) and were found to be 1.5 and 3.0 mg/cm^2. The targets were stored under vacuum before use in the experiment to avoid any oxidation from occurring [26, 27]. Below are the properties of the ^{144}Sm target used in this work:

- Isotopic Purity : 85.91 %
- Molecular weight : 150.36 g/mol
- Appearence : Yellow metal, tarnishes on exposure to air and forms an oxide
- Stability : Stable
- Melting Point : 1072 °C

- Boiling Point : 1791 °C
- Solubility : Insoluble in water
- Specific gravity : 7.536 g/cm^3
- Storage: Store in a closed container; in a cool, dry, well ventilated, low fire-risk area. Protect container from physical damage.

Table. 3.1. *Isotopic analysis of Samarium (Sm). It shows the composition of the Samarium target used.*

Isotope (Sm)	**Atomic Percent**	**Precision plus/minus**
144	85.91	0.21000
147	3.88	0.02000
148	2.18	0.02000
149	2.19	0.04000
150	1.02	0.02000
152	2.80	0.06000
154	2.08	0.04000

3.4.2 The AFRODITE Array

AFRODITE is an acronym which stands for **AFR***ican* **O***mnipurpose* **D***etector* for **I***nnovative* **T***echniques* and **E***xperiments* [28]. AFRODITE is a medium-sized array composed of two types of high purity germanium (HPGe) detectors; clover detectors and low energy photon spectrometer (LEPS) detectors. Figure 3.7 shows the AFRODITE array. The AFRODITE has a rhombicuboctahedron shaped aluminium frame with 16 detector positions. At the center of the AFRODITE array is a target chamber shown Figure 3.8 with the same geometry as that of a support frame and has thin (75 micron) Kapton windows on the 16 square faces. Detectors can be placed at 45°, 90° or 135° with respect to the beam direction as indicated in Figure 3.9. The clover detectors are surrounded by bismuth germanate ($Bi_4Ge_3O_{12}$) detectors known as BGO shields.

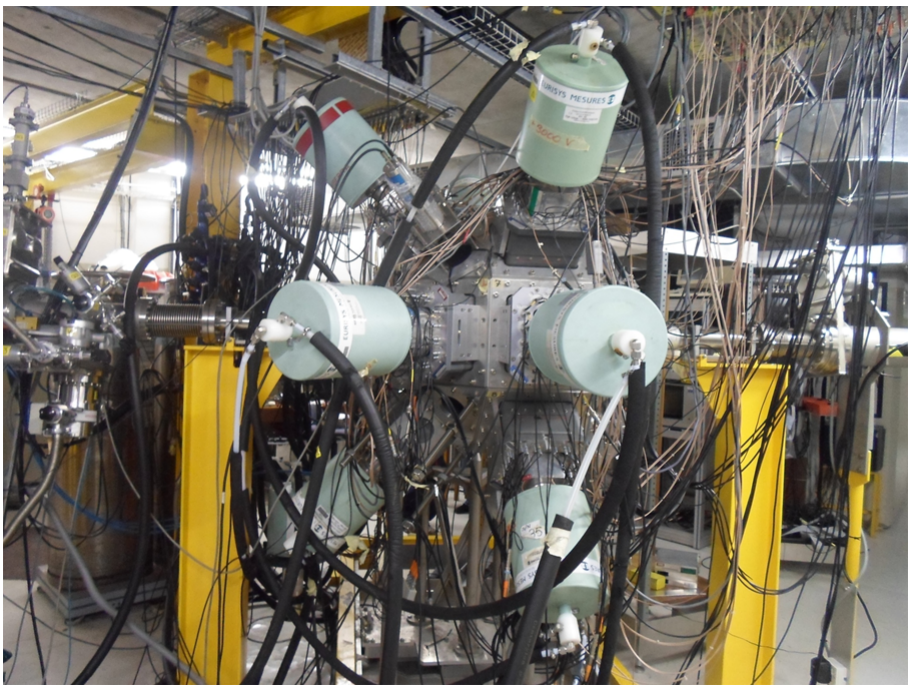

Figure 3.7: *AFRODITE array at iThemba LABS, with clover and LEPS detectors.*

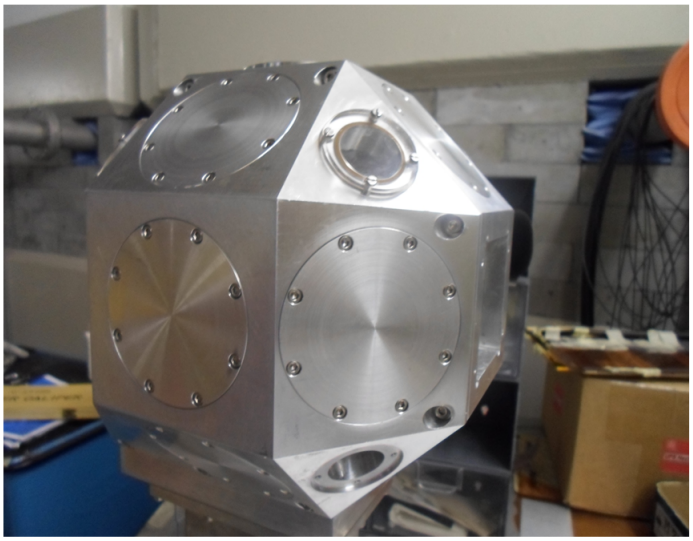

Figure 3.8: *Target chamber, at the center of the AFRODITE array.*

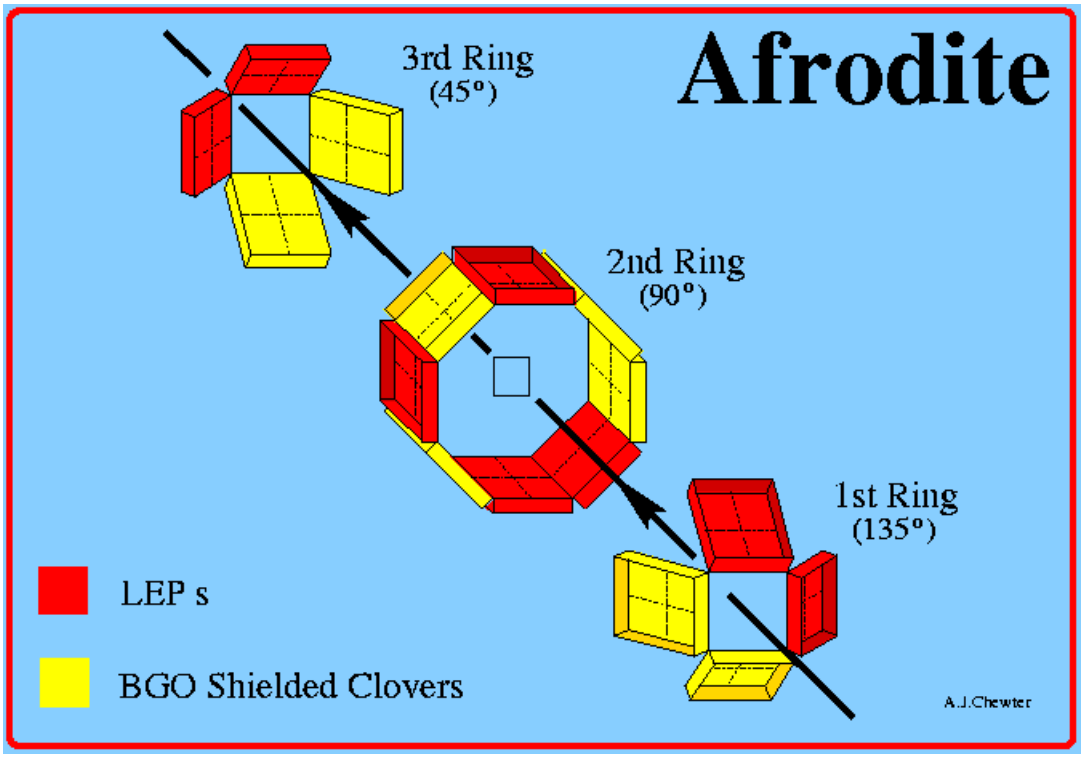

Figure 3.9: *Schematic drawing showing the three detector rings and possible arrangement of the detectors with the angles at which they can be placed [29].*

The combination of the clover detectors and LEPS detectors gives AFRODITE the unique capability to detect both high and low energy photons with a reasonably high efficiency, and with BGO shields enhancing sensitivity by reducing background. The characteristics of the clover detectors and BGO shields are explained in detail below.

Clover Detectors

The AFRODITE array has nine clover detectors that are essential for the detection of high-energy photons. Each clover detector consists of four n-type coaxial HPGe crystals that are 0.2 mm apart. The crystals have the dimensions of 70 mm length, 50 mm front diagonal length, 41 mm front width and 36 mm tapering length. The dimensions of the crystals are clearly shown in Figure 3.10 [33].

The four crystals are arranged in a common cryostat with tapered rectangular shape (see Figure 3.11) . Each crystal has its own electronics connection to ensure independent output

signals. This granular arrangement helps with the possibility of addback and this results in better photopeak efficiency and reduction of Doppler broadening of the peaks. Figure 3.12 shows the schematic cross section of the Clover-BGO system. The detectors need to be kept at temperatures of approximately -180 °C in order to reduce leakage current which may damage detectors. Therefore, the detectors are connected to an automated liquid nitrogen cooling system which monitors and keep the individual detectors at the desired temperature. The liquid nitrogen tanks, shown in Figure 3.13, are connected to the liquid nitrogen dewars (see Figure 3.11) of the detectors through the PolyTetraFluoroEthylene (PTFE) tubes to cool down the detectors.

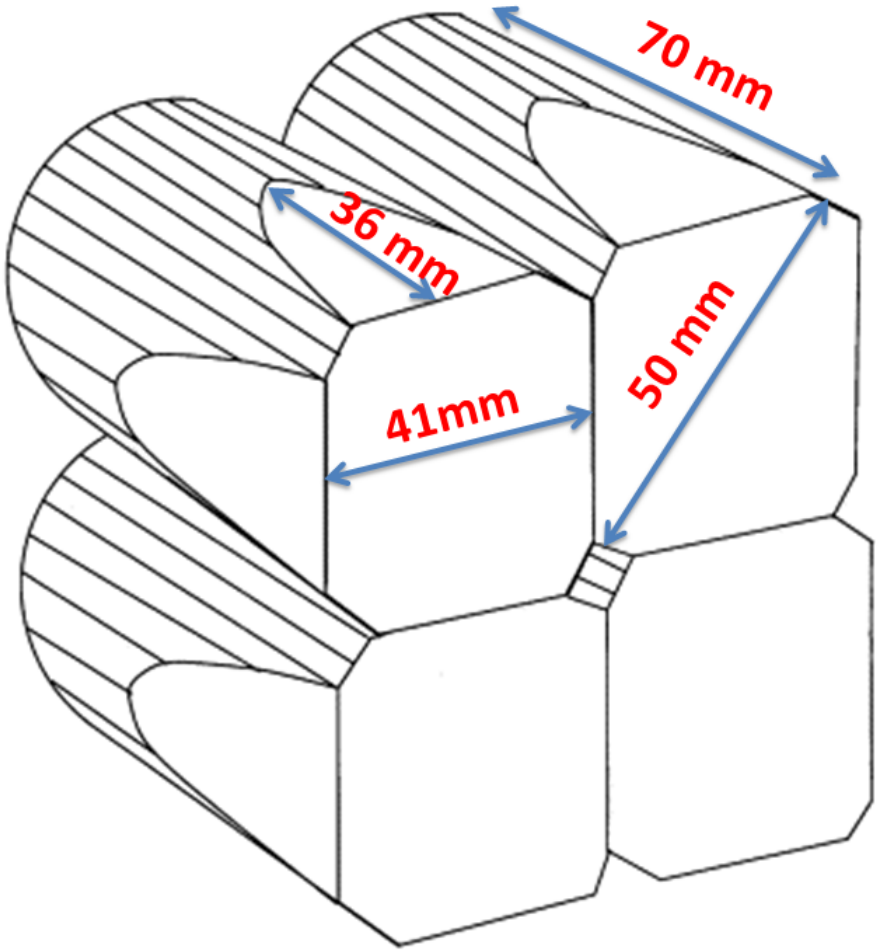

Figure 3.10: *Schematic representation of the four crystals of a clover detector [33].*

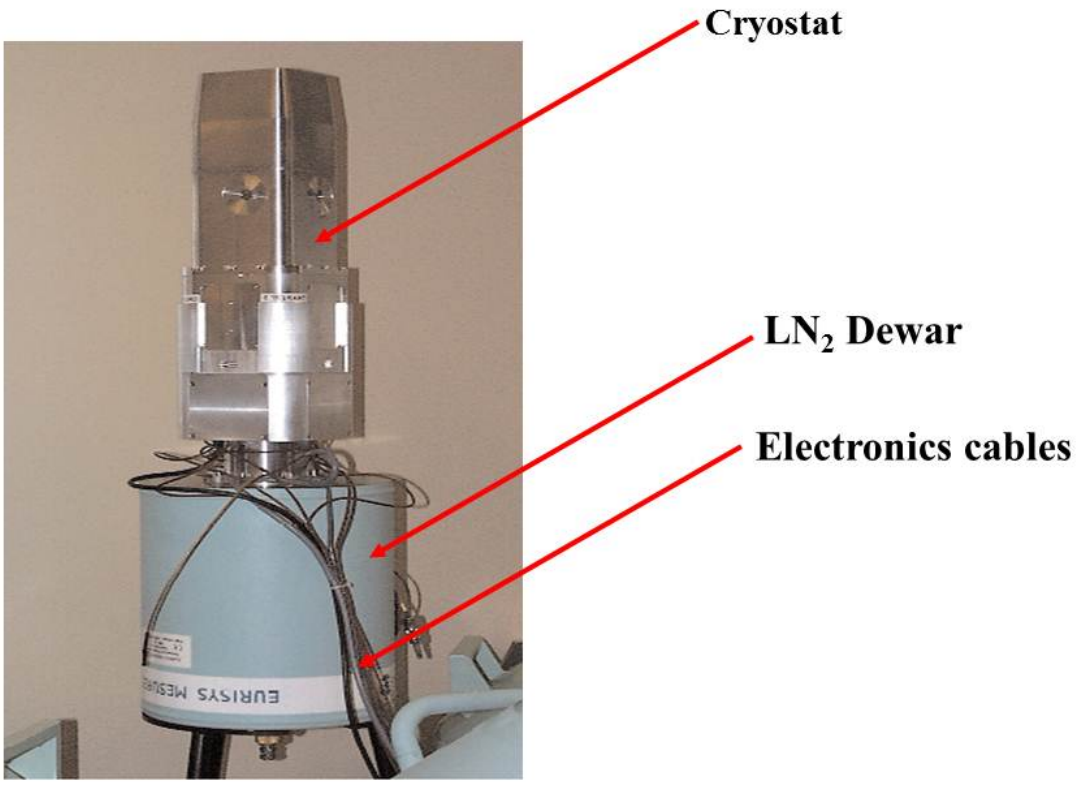

Figure 3.11: *Picture of a clover detector, it shows the liquid nitrogen dewar, electronic cables and the tapered rectangular cryostat [30].*

Each detector is constructed with an integral 2.5 litre liquid nitrogen dewar, see Figure 3.11, which in turn is coupled to the sensitive crystals by means of a copper rod for continuous cooling. The detectors are filled via insulated PTFE tubes and solenoid-operated valves, from a 180 litre liquid nitrogen supply tank, shown in Figure 3.13. The filling sequences and times are controlled by a programmable logic controller, while the supply tank volume is monitored by means of a load-cell scale with a digital readout unit. The detector temperatures are monitored by an electronic alarm system, as well as a graphic temperature display and temperature history on a dedicated computer. The liquid nitrogen dewars of the clover detectors are filled every 12 hours by an automated filling system [**?**].

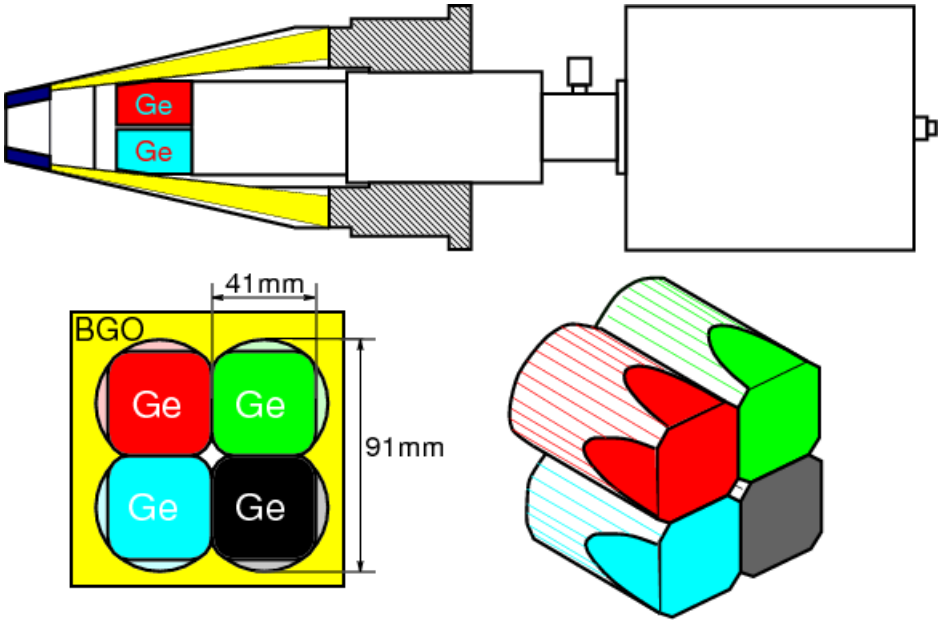

Figure 3.12: *Schematic drawing of the germanium detector surrounded by the BGO shield. It also shows the four crystals of the detector and its dimensions [31].*

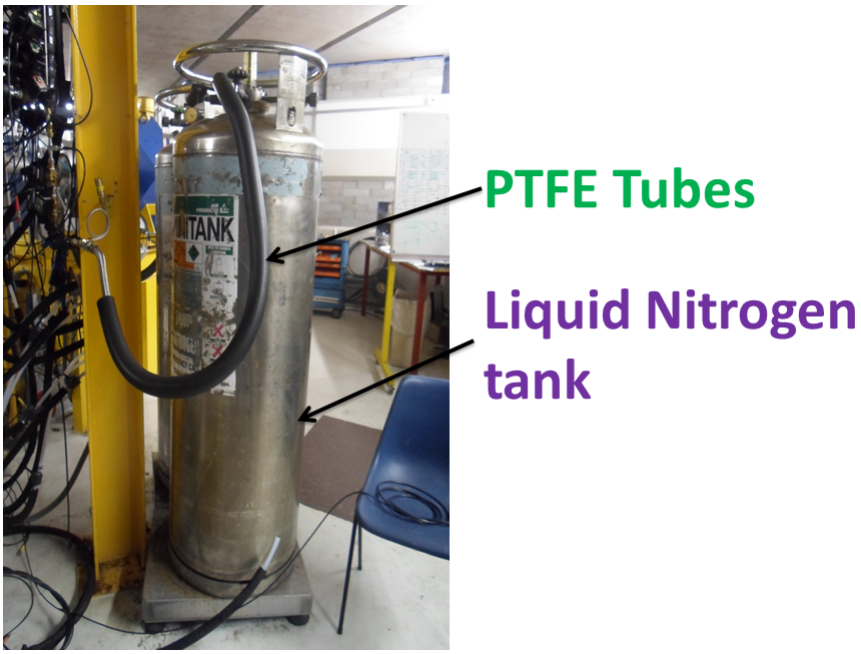

Figure 3.13: *Liquid Nitrogen tanks connected to the liquid nitrogen dewars of the detectors through the PTFE tubes (black tubes on the picture) to cool down the detectors.*

Some specifications of the clover crystals [32]:

- Distance between the crystal surface and the target centre: D_{tc} = 196 mm
- Distance between the detector end-cap and the crystal surface : D_{ec} = 20 mm
- Total opening angle: $\Theta = 23.2°$
- Solid angle per detector: $\Omega_{Ge} = 1.34$ % of 4π (for a 0.2 mm distance between crystals)
- Photo-peak efficiency (for 1.33 MeV): $\varepsilon_{ph}\ \Omega_{Ge} = 17.8 \times 10^{-4}$
- Add-back factor (for 1.33 MeV): 1.56
- Peak-to-total ratio (for 1.33 MeV): $(P/T)_{Ge} = 0.30$

The following are the advantages of the clover detectors [34]:

- The crystals have smaller opening angles and this reduce doppler broadening of the peaks.
- Good energy resolution
- Good timing response
- High sensitivity to the linear polarization of γ rays due the four crystals that act as polarimeter.

BGO Shields

The bismuth germanate (BGO) detectors are Compton supressor shields for germanium detectors. The clover detectors are each surrounded by a BGO shield to reduce background. Figure 3.14 shows BGO suppression shields around the clover detector. Because of its high atomic number ($Z_{Bi} = 83$), BGO has high stopping power which makes it a good material for a Compton suppressor shield. It can be seen in equation 3.8 that the stopping power is directly proportional to the atomic number Z, therefore, large atomic number results in high stopping power [6].

$$\frac{dE}{dx} = (\frac{e^2}{4\pi\epsilon_0})^2 \frac{4\pi z^2 N_0 Z_\rho}{mc^2\beta^2 A}[\ln(\frac{2mc^2\beta^2}{I}) - \ln(1-\beta^2) - \beta^2] \tag{3.8}$$

Gamma rays can either fully deposit their energy or be scattered out of the HPGe crystals, as discussed in Section 3.2.1. The scattered γ rays contribute to the unwanted Compton background. The BGO shield detects γ rays that are scattered out of HPGe crystals without depositing their full energy and, thereby, they help in reducing the background.

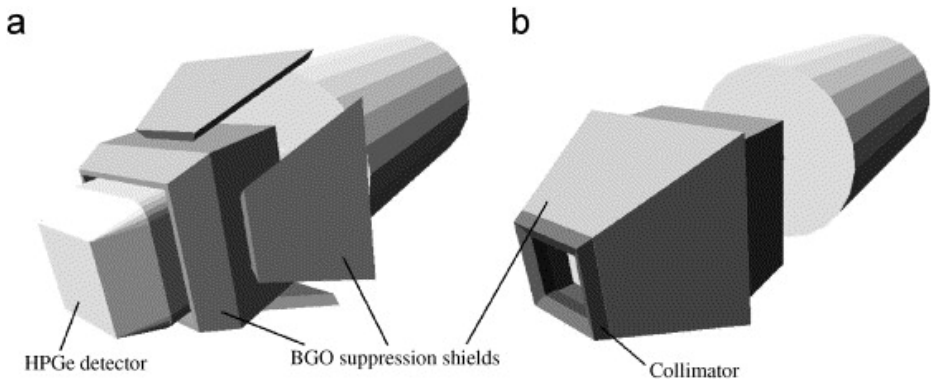

Figure 3.14: *Picture showing the BGO shields around the germanium detector [35]. a shows the HPGe detector inside the suppression shields and b clearly shows the suppression shields that surrounds the detector and the collimater in the front.*

3.4.3 Experimental Method

As mentioned earlier, the experiment was performed using the AFRODITE array at iThemba LABS[1] near Cape Town, South Africa. The plan view of the iThemba LABS facilities is shown in Figure 3.15 and the AFRODITE array is located at on a beam line F. Table 3.2 gives the description of the abbreviations used in Figure 3.15. At iThemba LABS, heavy ion beams are prepared in the Electron Cyclotron Resonance Ion Source (ECRIS) then injected in the second injector cyclotron (SPC2) through the AX line. At SPC2 the beam is preaccelerated to an energy of about 8 MeV then directed to the SSC through the K line. In the SSC the beam is accelerated to the desired energy as required by the physics users. For the present experiment the beam of α particles was accelerated to the energy of 26.3 MeV. From the SSC the beam was directed to the AFRODITE vault through the beam lines X, P1, R and F, as indicated in Figure 3.15.

Four weekends[2], each with 8 shifts[3], of beam time were allocated for the present experiment. The first two weekends[4] were performed using the analog system and in the last two[5] weekends the digital system was used. The first two weekends of the analog system did not give enough statistics and, therefore, two weekends of the digital system were proposed in order to improve the data statistics. It is worth mentioning that this experiment was the first ever to be performed using the new digital system at iThemba LABS.

[1] iThemba Laboratory for Accelerator Based Sciences
[2] Each weekend is from Friday 16:00pm to Monday 08:00am
[3] Each shift is 8 hours
[4] 25-28 Nov 2011 and 02-05 Dec 2011
[5] 06-09 July 2012 and 24-07 August 2012

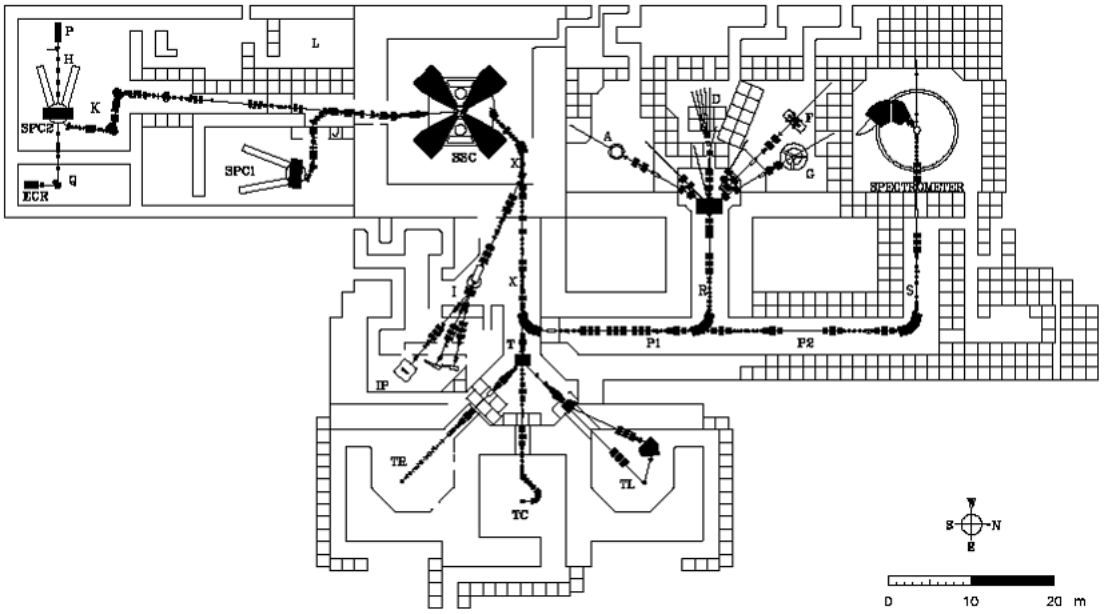

Figure 3.15: *Plan view of the facilities at iThemba LABS [36].*

Table. 3.2. *Description details for abbreviations used in Figure 3.15.*

Abbreviation	**Description Detail**
A	Scattering Chamber beam line
D	Collimated neutron beam facility
ECR	Electron Cyclotron Resonance Ion Sources
ECD	Electron and Cable Distribution
F	AFRODITE γ ray spectrometer
G	γ ray angular correlation table
IP	Isotope Production
L	Low energy experimental area
P	Polarized Ion Source
SPC1	Solid pole injector cyclotron for light ions
SPC2	Solid ion cyclotron for heavy and polarized ions
SSC	Separated Sector Cyclotron
TC	Isocentric system for neutron therapy
TR	Horizontal beam line for proton therapy
TL	Isocentric proton therapy

Before each experiment is performed the most important thing is to choose the suitable beam-target combination for populating the desired states in a nucleus of interest at optimum cross-section. To achieve this, statistical model calculations are normally performed using PACE (Projected Angular Momentum Coupled Evaporation). The PACE program predicts the suitable beam energy for the experiment. The optimum beam calculations were done from the measurements by Yates *et al.* [37, 38]. From this measurement an optimum beam energy was found to be 26.3 MeV for a ^{144}Sm (α,2n)^{146}Gd fusion evaporation reaction to study the non-yrast states in ^{146}Gd. The experiment was set to measure $\gamma - \gamma$ coincidences. For the four weekends, both that of the analog and that of the digital system, eight clover detectors[6] were used, with 4 clover detectors placed at 135° and the other 4 at 90°. Below are the steps that were followed when performing the experiment:

- Before the $\gamma - \gamma$ coincidence measurents were taken, first the ^{56}Co and ^{152}Eu sources were put inside the target chamber (target position), one after the other, for energy calibration.
- Thereafter the ^{144}Sm target, enriched to 85.91%, of 3.0 mg/cm^2 thickness was placed in a target ladder, shown in Figure 3.16, and was mounted inside the target chamber.
- Absorbers (0.15 mm Tin and 0.07 mm Brass) were placed in front of the detectors to reduce count rate due to the X-rays. They were differently placed in front of different clover detectors, i.e. Tin in the other detectors and Brass in the others.
- 21 mm Copper absorbers were put, instead of Tin and Brass, in front of the clover detectors.
- During weekend 3 and 4 the beam of α particles was supplied by the Separated Sector Cyclotron (SSC) and was accelerated to the AFRODITE vault through beam lines X, X, P1, R and F indicated in Figure 3.15. The location of the SSC and the AFRODITE vault can be seen in the plain view of the facilities at iThemba LABS as shown in Figure 3.15.

[6]Note that only eight clover detectors were used and the ninth was away for repairs. The LEPS detectors were not used because the focus of this study was in the high energy region and the LEPS detectors are significant for low-energy photon detection.

- The target nucleus was bombarded with the beam of α particles, and through the fusion-evaporation reaction the ^{146}Gd nucleus was produced.
- The γ rays were detected using the AFRODITE array.
- At the end of the in-beam experiment the ^{144}Sm target was removed from the chamber, the ^{56}Co and ^{152}Eu sources were mounted in a target chamber (target position) to collect data for efficiency calibration.
- The collected data were saved on the magnetic Digital Linear Tape (DLT) for off-line analysis later.

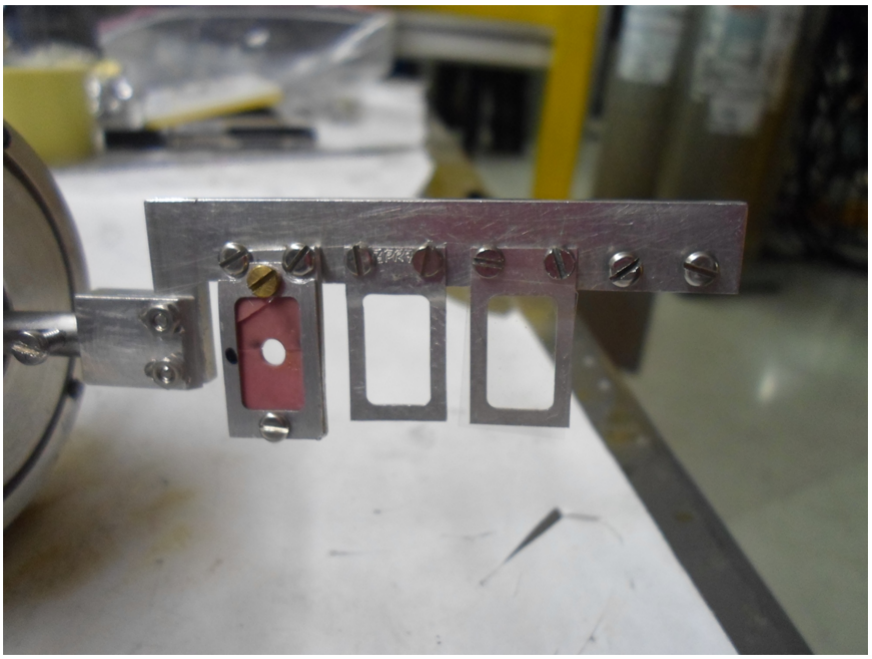

Figure 3.16: *Picture of the target ladder with a hollow ruby in place. The target ladder can accomodate four target frames.*

Table 3.3 and 3.4 show the summarised information of the four weekends[7].

Table. 3.3. *PR189: First two weekends of analog system.*

	Weekend 1	**Weekend 2**
Beam Particle	$^{4}_{2}$ He (α)	$^{4}_{2}$ He (α)
Beam Energy	26.3 MeV	26.8 Mev
Pulsing	16.279 MHz 61.4 ns	16.279 MHz 61.4 ns
Target Nucleus	^{144}Sm	^{144}Sm
Target Thickness	3.0 mg/cm^2	3.0 mg/cm^2
Absorbers	0.15 mm Tin 0.07 mm Brass	0.15 mm Tin 0.07 mm Brass
Trigger	$\gamma - \gamma$	$\gamma - \gamma$
Clover positions	4 at 90° 4 at 135°	4 at 90° 4 at 135°
Beam Current	between 19 nA ad 25 nA	between 24 nA and 29 nA
Count Rate	between 10 k.s^{-1} and 22 k.s^{-1}	between 16 k.s^{-1} and 30 k.s^{-1}

Table. 3.4. *PR200: Second two weekends of digital system.*

	Weekend 3	**Weekend 4**
Beam Particle	$^{4}_{2}$ He (α)	$^{4}_{2}$ He (α)
Beam Energy	26.1 MeV	26.7 MeV
Pulsing	16.271 MHz 61 ns	16.278 MHz 61 ns
Target Nucleus	^{144}Sm	^{144}Sm
Target Thickness	3.0 mg/cm^2	3.0 mg/cm^2
Absorbers	21 mm Cu	21 mm Cu
Trigger	$\gamma - \gamma$	$\gamma - \gamma$
Clover positions	4 at 90° 4 at 135°	4 at 90° 4 at 135°
Beam Current	between 15 nA ad 18 nA	between 17 nA and 49 nA
Count Rate	between 16 k.s^{-1} and 38 k.s^{-1}	between 16 k.s^{-1} and 96 k.s^{-1}

[7]Please note that the count rate in the tables is per each clover detector.

3.5 Data Acquisition System And Electronics

The basic principle for the detection of any particle is that it interacts with the detector medium and the interaction will cause electrical pulses in the detector. The electrical signals contain the information about the detected particle, information such as particle type, energy, time distribution, etc. These electrical signal are processed by experimenter-configured electronics. After the signal has been processed the obtained information is then presented to the CAMAC[8] (CAMAC is the clover module that contains the electronics to control a clover detector, all germanium detectors energies and times, together with BGO suppression) modules for digitization and the information is read out by the front-end data acquisition software.

Data from this work was collected using two types of data acquisition systems; analog and digital. As mentioned before, the first two weekends of analog system did not give enough statistics and, therefore, extra data were collected with the digital system. The digital system has less dead time (dead time is the time after each event during which the system is not able to record another event [39]) compared to the analog system and for that reason it can record more data than the analog system. In the next section, the two data acquisition systems are briefly explained, starting from the front-end of each system.

3.5.1 Analog Data Acquisition System

The data acquisition front-end of the analog system consisted of a Versa Module Europa (VME)-based processor module, which runs experimenter-configured tasks under the pSOS[9] + real time kernel. This front-end data acquisition reads out the digitized event data from CAMAC modules. From the VME front-end the event streams are read by the VAX[10] workstation over the ethernet network. The VAX workstations, running the XSYS data acquisition software under VMS operating system, perform online data sorting, histogramming, display and event taping. Stored data can be sorted using MIDAS[11] MTsort,

[8] CAMAC - Computer Automated Measurement And Control
[9] Portable Software on Silicon (PSOS) is a real time operating system
[10] VAX - Virtual Address eXtension
[11] MIDAS - Multi Instance Data Acquisition System

which is a sorting program, and the input handler[12] to be chosen for online sorting is AfroditeOnlineTS and AfroditeDisc for offline sorting.

3.5.2 Digital Data Acquisition System

The data acquisition front-end of the digital system consisted of the PXI crate, XIA cards which are connected to server PC which runs the data-acquisition process and data collection modules. DDAS (Digital Data Acquisition System) also has the control part on server PC which runs the merge, filter, event-building, online sorting, storage and GUI (Graphic Unit Interface). The merge processer receives data from the merge to the filter/ event-builder. Data are read from merger and output to TapeServer. The TapeServer receives and store data locally, either on disc, USB, network, Tape, etc. The stored data can be sorted with MIDAS MTsort, and the input handler to be chosen is EurogamOnlineTS for online sorting and EurogamDisc for offline sorting [40].

3.5.3 DDAS Set Up

As mentioned previously, this experiment was the first at iThemba LABS to be performed using the new digital system and, therefore, before the experiment was performed, parameters had to be optimized[13]. With the ^{152}Eu source on the target chamber parameters were varied to see which ones gave better resolution compared to that of the previously used analog system. On the 24^{th} and 25^{th} of of June 2012 an α in-beam experiment dedicated to the digital system test was performed. The ^{197}Au target was bombarded with α beam at an energy of 52 MeV to produce the ^{197}Tl nucleus. Both systems were used at the same time to collect data. The data obtained were sorted and the results were compared.

The main parameter to optimize energy resolution is the energy filter rise time. Generally, long rise times give better resolution, but it reduces the throughput (output period of time). The trigger threshold should be set as low as possible for best resolution. However, if it is too low it results in detecting unwanted events, increasing input count rate drastically. If the threshold is too high, especially at high count-rates, low-energy events below the

[12]Input handler is found on the MTsort Run Window of MIDAS
[13]This was done with the help of Dr. P. Jones, Siyabonga Majola and Vincent Kheswa.

threshold can pass the pile-up inspector and pile up with other events. This increases the measured energy and thus leads to exponential tails on the (ideally Gaussian) peaks in the spectrum. Ideally, the threshold should be set such that the noise peaks just disappear. The settings of the trigger filter do not have much effect on the resolution, but changing the trigger conditions might result in undesirable peak shapes. A longer trigger rise time allows the threshold to be lowered more, since the noise is averaged over longer periods. This helps to remove tails on the peaks. A long trigger flat top will help to trigger better on slow rising pulses and thus resulting in a sharper cut off at the threshold in the spectrum.

The preamplifier decay time, tau (τ), is used to correct the energy of a pulse sitting on the falling slope of a previous pulse. The calculations assume a simple exponential decay with one decay constant. A precise value of τ is especially important at high count rates where pulses overlap more frequently. If τ is off the optimum, peaks in the spectrum broaden, and if τ is wrong, the spectrum will be significantly blurred. The best way of finding the best value of τ is exploring through different values of τ at high count rates as the effect on the resolution is more pronounced and this value will also be valid for low count rates [41]. Figure 3.17 shows DDAS parameter set up window, with all the parameters that can be varied to optimize the system.

Before the α in-beam test, the digital system was tested using a ^{60}Co. The ^{60}Co source was put in the front of the clover detectors. The data were collected for different values of τ. For each value of τ, the peak sample was changed to see which value of τ gives almost the same value of the peak postion for different peak sample values. On the ^{60}Co spectrum the peak position (centroid) of the 1332.5 keV peak was checked to see if it changes as the peak sample value is changed, for each value of τ. The anticipated value of τ was the one which would give almost the same, or better yet the same, value of the peak position for different values of the peak sample; i.e the centroid of the 1332.5 keV peak should be the same for different peak sample. From this test it was found that the value of τ that gave better results is $\tau = 25$ μs. Figure 3.18 is the graph showing how the peak position changes as the peak sample is varied for different values of τ. In Figure 3.18 it can be seen that $\tau = 25$ μs gives better results compared to the others; the peak position does not change much for different peak sample values.

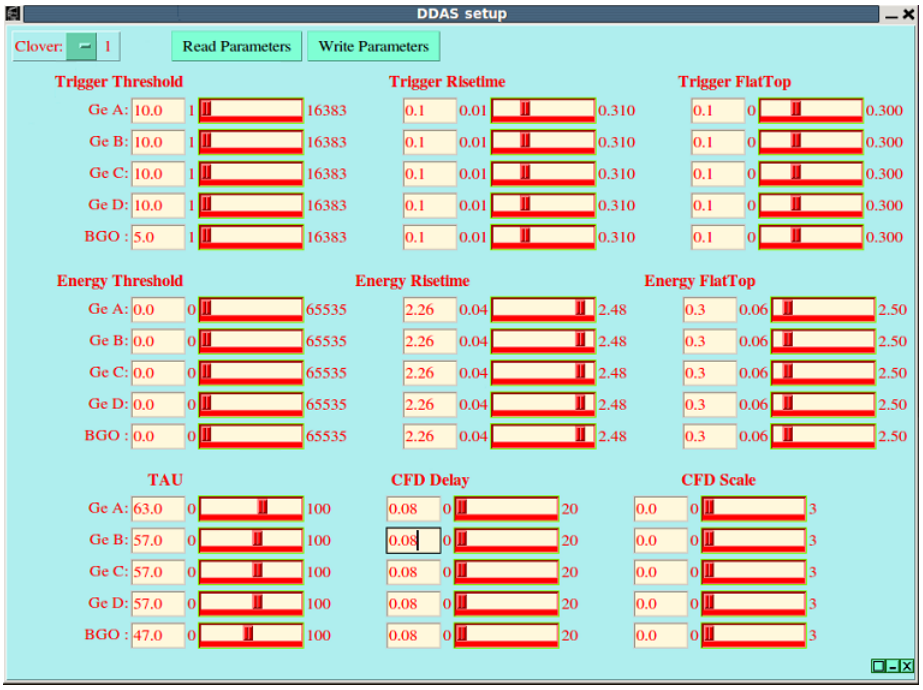

Figure 3.17: *Picture of a DDAS set up window, showing different parameters that can be changed to optimize the system for better resolution.*

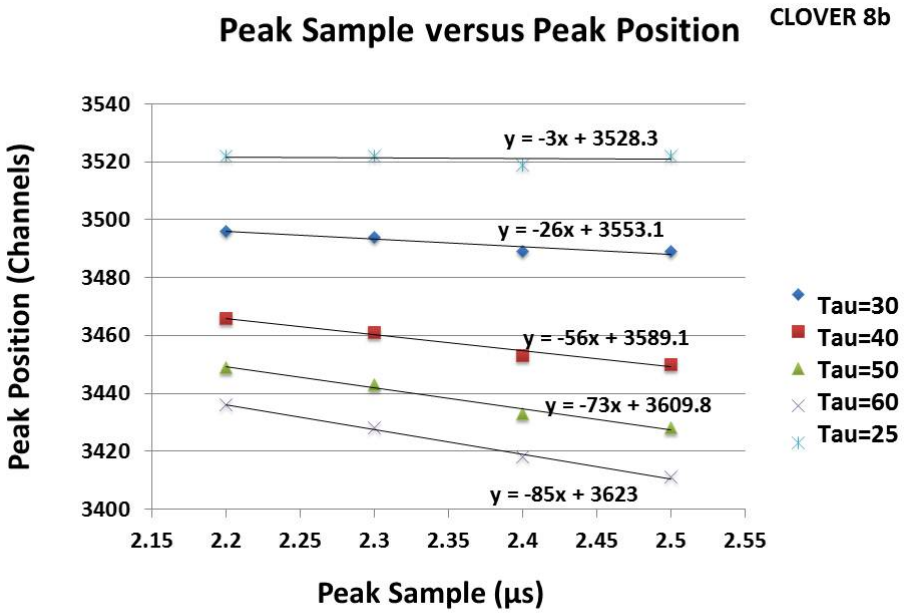

Figure 3.18: *Graph of the peak position versus peak sample for different values of τ.*

Now, using this value of tau ($\tau = 25\ \mu$s) the ^{152}Eu source was used to compare the resolution of the digital and the analog system. With the ^{152}Eu source in front of the detectors the data was collected, using both analog and digital respectively system, for about an hour. The peaks of the ^{152}Eu source were fitted to get their full-width half maximum (FWHM) so that the energy resolution can be calculated using equation 3.9.

$$Resolution = B * FWHM \tag{3.9}$$

where B is the parameter obtained when fitting the peak. Tables 3.5 and 3.6 show the results obtained from both the analog and the digital system.

Table. 3.5. *Resolution of the ^{152}Eu peaks. Data collected with the analog system.*

Clover crystal	Peak Energy	B	FWHM	Resolution
A	121.78	0.547	3.86	2.113
	244.69		3.97	2.171
	344.27		4.03	2.204
	1408.01		4.90	2.679
B	121.78	0.243	7.835	1.908
	244.69		7.92	1.928
	344.27		8.32	2.026
	1408.01		11.14	2.712
C	121.78	0.276	6.645	1.89
	244.6		6.90	1.910
	344.27		7.06	1.955
	1408.01		9.58	2.652
D	121.78	0.260	5.960	1.552
	244.6		6.23	1.622
	344.27		6.34	1.651
	1408.01		6.89	1.791

The results shown in Tables 3.5 and 3.6 and the graph in Figure 3.19 clearly shows that the digital system has better resolution than the analog system. This also confirms that indeed the decay constant value ($\tau = 25\ \mu$s) is optimum.

Table. 3.6. *Resolution of the ^{152}Eu peaks. Data collected with the digital system.*

Clover crystal	Peak Energy	B	FWHM	Resolution
A	121.78	0.377	5.39	2.032
	244.69		5.33	2.009
	344.27		5.54	2.088
	1408.01		6.74	2.541
B	121.78	0.379	4.49	1.702
	244.69		4.67	1.770
	344.27		4.80	1.819
	1408.01		5.93	2.247
C	121.78	0.361	5.80	2.094
	244.6		5.72	2.064
	344.27		6.09	2.198
	1408.01		7.0	2.527
D	121.78	0.815	3.23	2.632
	244.6		3.22	2.624
	344.27		3.23	2.632
	1408.01		3.77	3.072

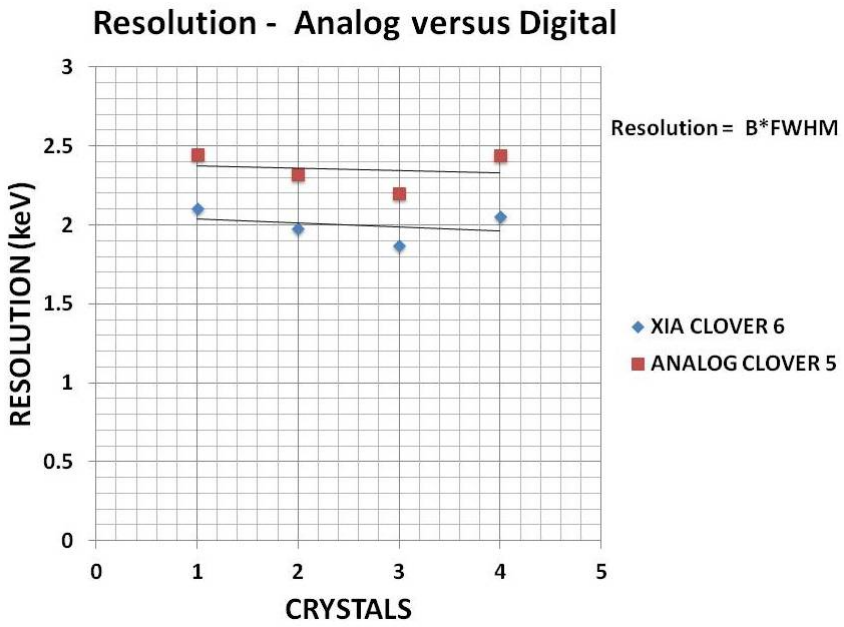

Figure 3.19: *Graph comparing the measured energy resolution using the analog and digital systems.*

The obtained parameters that were thought to be optimum were then used in an in-beam experiment, which was dedicated to the DDAS test. During this in-beam experiment the beam current was varied between 10 nA - 100 nA to investigate which one gave more count rate. Table 3.7 shows the clover count rates for both analog and digital system for different beam currents. The clover count-rate for the digital system is higher compared to that of the analog system, but for the analog system the rate increases as the beam current increase from 10 nA to 100 nA, whereas for the digital system the count-rate only increases up to a beam current of about 60 nA and then it decreases at beam current higher than 60 nA (see Table 3.6).

Table. 3.7. *Table showing clover count rates for different beam currents (from 10 nA to 100 nA). Clover Count Rate -A is the count rate collected with the analog system and Clover Count Rate -D with the digital system.*

Beam Current (nA)	Clover Count Rate ($k.s^{-1}$) - A				Clover Count Rate ($k.s^{-1}$)- D			
	C1	C3	C5	C7	C1	C3	C5	C7
10	6.5	7.5	9.0	9	13.2	12.4	12.8	12.4
20	13	13	18	18	29.6	25.2	23.6	23.6
30	14.6	14.5	19	18	30.4	24.5	24.5	26.8
40	17	16	22	21	30.4	31.6	37.2	33.6
53	24	22.5	30	32	32.8	33.6	36	32.4
60	26	25	36	36	34.4	33.6	29.2	29.2
70	30	28	38	40	31.2	28.8	31.2	28.0
80	38	35	50	50	30.4	27.6	30.4	30
90	42	40	58	56	31.2	28.4	26.8	26.4
100	45	45	62	62	28.8	30.4	28.4	26.0

Below are the results from the digital test experiment (in-beam) that was performed. The experiment was to test if the obtained parameters will still give good resolution at high count rates. It was also to check the effect of the beam current on the count rate and energy resolution. Figures 3.20 and 3.21 are the spectra for both digital and analog at a beam current of 14 nA and Figures 3.22 and 3.23 at a beam current of 28 nA. The results indicate that the digital spectra have more counts than the analog. When the beam intensity was increased to 28 nA, the digital system still collected more data than the analog system, as it can be seen from Figure 3.22 that the spectrum from the digital system has more counts than that from the analog system.

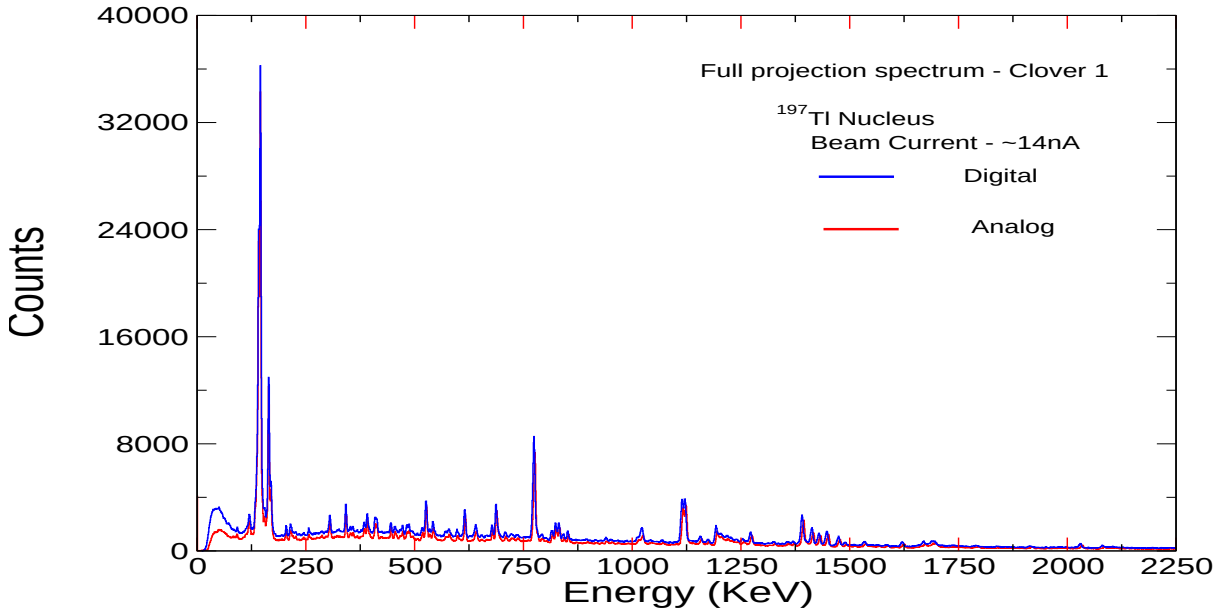

Figure 3.20: ^{197}*Tl full projection spectrum for the digital and the analog system at 14 nA beam current.*

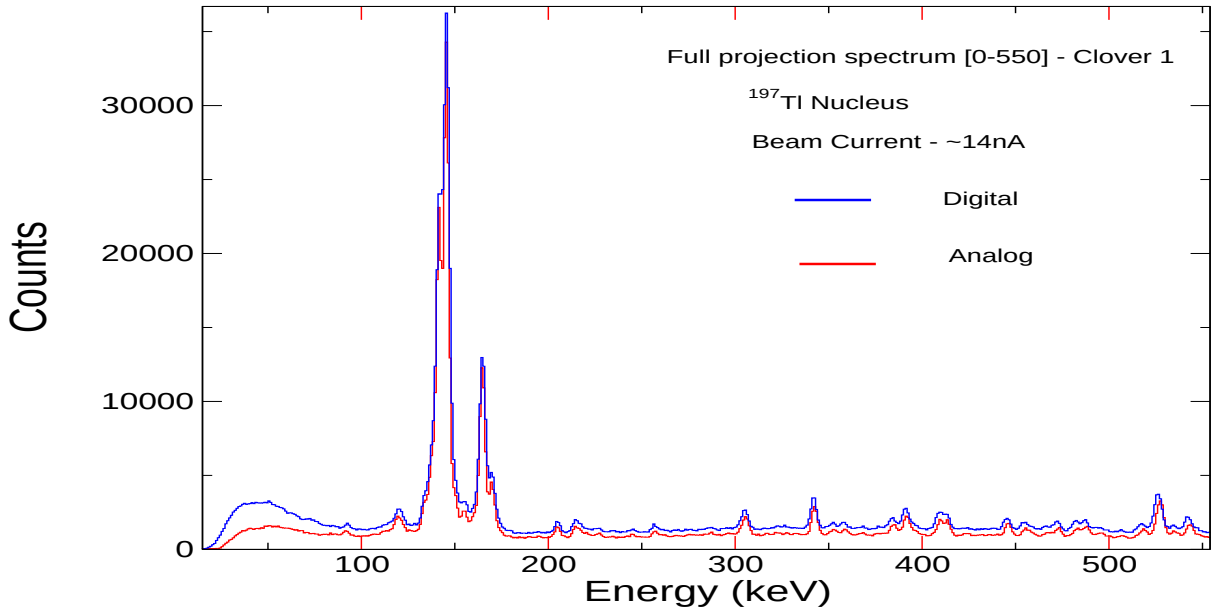

Figure 3.21: *The expanded spectra for the digital and the analog system. Showing more counts for the digital at 14 nA.*

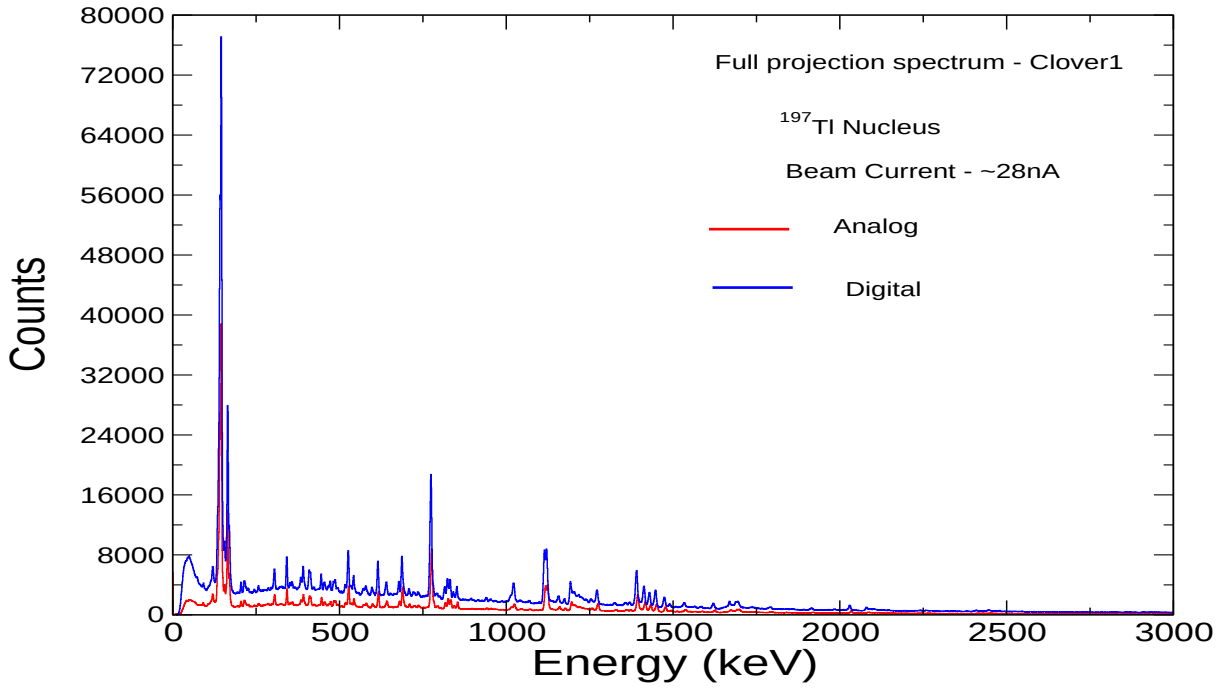

Figure 3.22: ^{197}*Tl full projection spectrum for the digital and the analog system at 28 nA beam current.*

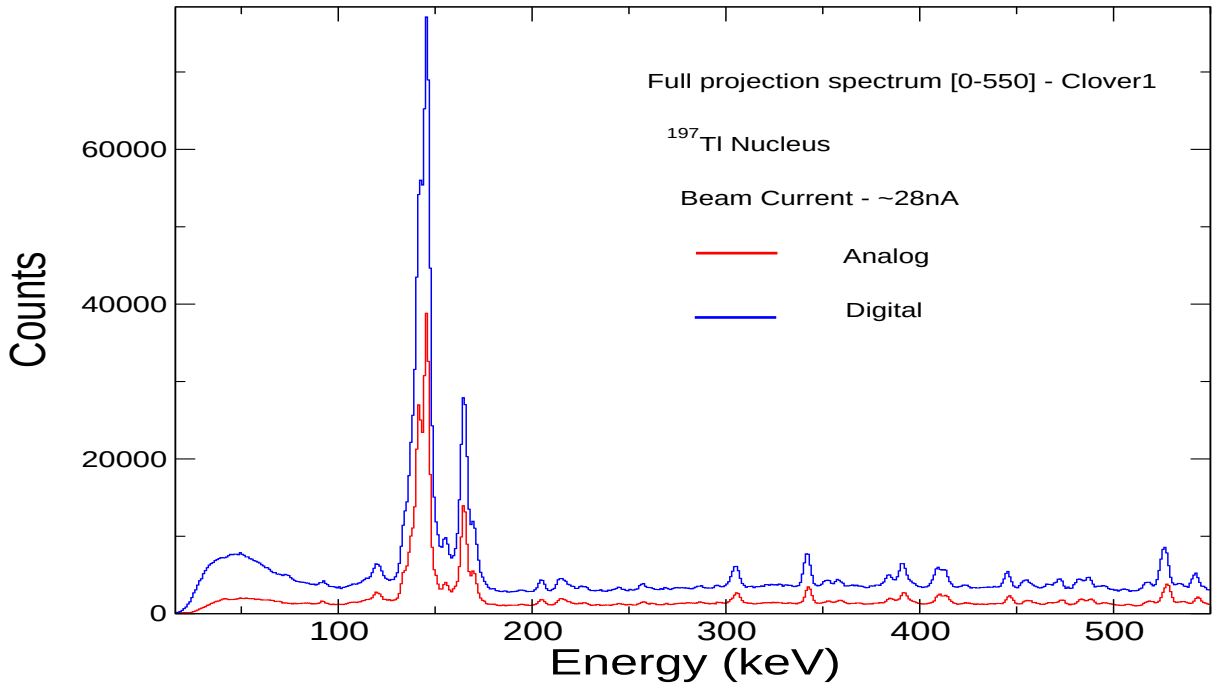

Figure 3.23: *The expanded spectra for the digital and the analog system. Showing more counts for the digital at 28 nA.*

Chapter 4

Data Analysis And Results

4.1 Introduction

This chapter discusses the methods used for data analysis and presents the results obtained from this work. It explains in detail the energy calibration of the detectors which was performed before each experiment and discusses the efficiency calibration of the detectors. The total projection, gated spectra and the partial level schemes derived from the 382 keV gated spectra are shown, both from this work and from previous work. The results obtained from this work are compared to the results from previous work [2]. Lastly, it discusses the setting of the limits and branching ratios.

4.2 Data Analysis Methods

4.2.1 Energy Calibration

When collecting γ ray events, the photopeaks are at certain channel numbers and channel numbers correspond to certain energies. In order to know the corresponding energies, energy calibration has to be done. Sources with well known energies, such as ^{133}Ba, ^{56}Co and ^{152}Eu, are used to calibrate the detectors. However, the relationship between the channel numbers and γ ray energies is not exactly linear, therefore, at the beginning the linear relationship was adjusted in software to give a dispersion of as 0.5 keV per channel.

Before each experiment single γ ray spectra were collected from the ^{56}Co and ^{152}Eu sources for energy calibration. Each source, one after the other, was placed on a target ladder and then put inside the target chamber at the target position. The data from sources were collected for about an hour each and were saved on disc. Figures 4.1 and 4.2 show the spectra obtained when using the ^{152}Eu and ^{56}Co sources respectively. For the analog system the SFIT program was used to determine the photopeak centroids from the two sources, ^{56}Co and ^{252}Eu. These centroids were then put into the SCAL program which then gives the energy calibration coefficients (a_0, a_1 and a_2) through the quadratic equation:

$$E = a_0 + a_1 x + a_2 x^2 \tag{4.1}$$

where x is the channel number. These coefficients are different for each and every crystal of the clover detectors. For the digital system the AUTOCAL program from MIDAS was used to get the energy calibration coefficients. These coefficients were then put in a sort code that was used to sort data from $\gamma - \gamma$ coincidence events.

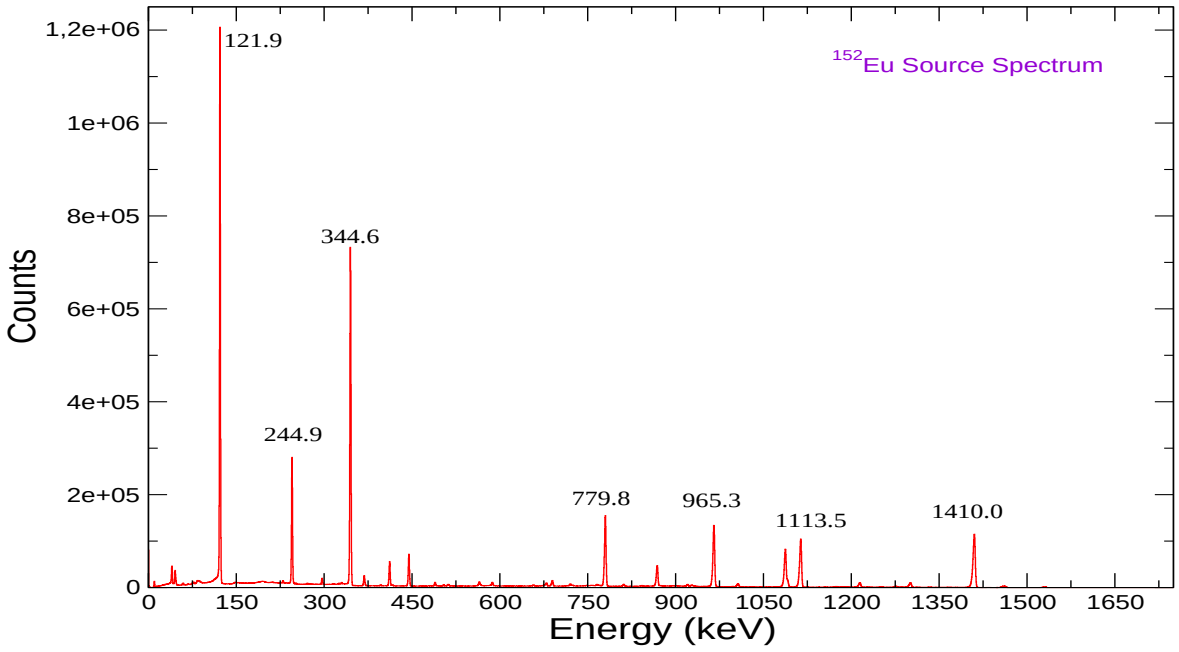

Figure 4.1: *Typical spectrum of the ^{152}Eu source used for energy and efficiency calibration.*

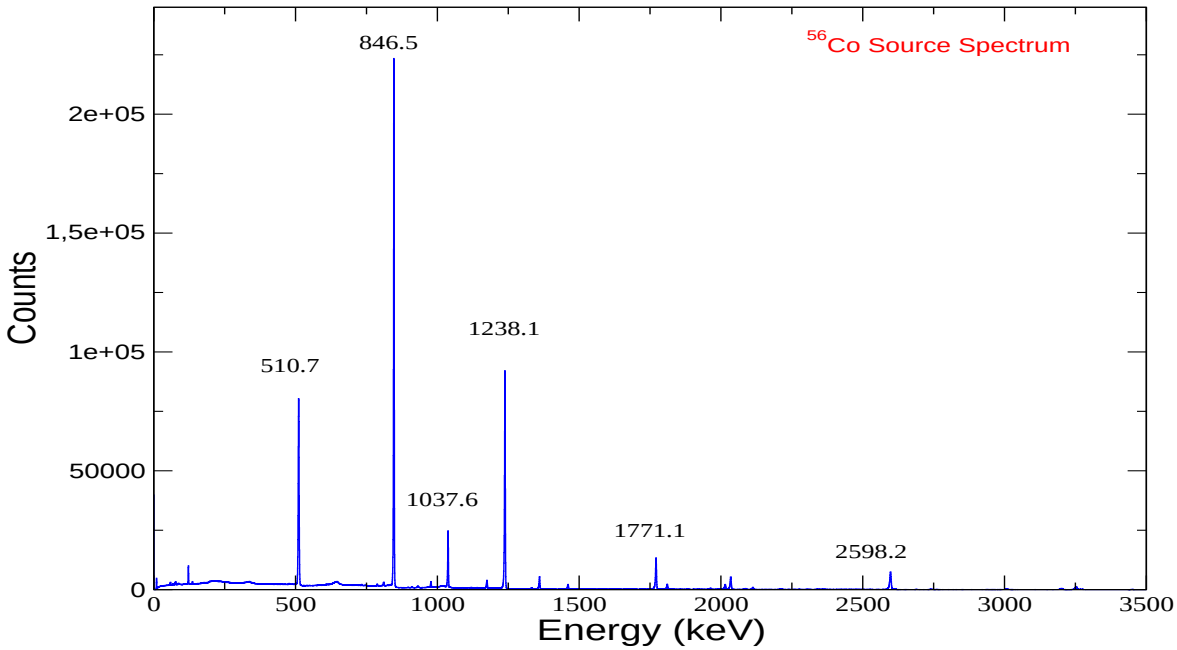

Figure 4.2: *Typical spectrum of the ^{56}Co source used for energy and efficiency calibration.*

4.2.2 Efficiency Calibration

Efficiency of the detector is the probability that an emitted γ ray will interact with the detector and produce an event. There are different types of efficiency definitions; absolute, intrinsic, relative and full-energy peak (photopeak) efficiency.

- Absolute efficiency - Ratio between the number of counts produced by the detector and the number of gamma rays emitted by the source in all directions.
- Intrinsic efficiency - Ratio between the number of pulses produced by the detector and the number of gamma rays striking the detector.
- Relative efficiency - Efficiency of one detector relative to another detector.
- Full-energy efficiency - The efficiency for producing full-energy peak pulses only, rather than a pulse of any size for the γ ray.

The detector efficiency depends upon the following things:

- Type of detector (HPGe, NaI, scintillation, plastic scintillation, liquid scintillation, etc.) and its response to ionization.
- Detector size and shape (larger areas and volumes are more efficient).
- The distance between the detector and the radioactive material.
- The radioisotope and type of radiation measured (alpha, beta and gamma radiation and their energies).
- The backscatter of radiation towards the detector (more dense surfaces produce more scattering)
- The absorption of radiation before it reaches the detector (by air and by the detector covering)

At the end of the experiment of each weekend, data from the ^{56}Co and ^{152}Eu sources were taken for efficiency calibration. The sources, one after the other, were put on a target ladder and were placed inside the target chamber in a target position. For efficiency calibration it is essential that the source be put in a target position. The collected data was then sorted using MIDAS MTsort.

The sorted data were then used to get the efficiency curves using the RadWare programs. Below are the few steps that were followed to plot an efficiency curve:

- Fit the peaks from the add-back total spectrum of the sources using the FT command on gf3. This gives areas of the fitted peaks and their corresponding centroids.
- The areas of the fitted peaks are stored in a .sto file.
- Run SOURCE to create the .sin file using the previously created .sto file and the .sou file from the demo files on Radware.
- The above steps are done for both sources (^{56}Co and ^{152}Eu), so this means there will be two .sin files.

- EFFIT the ^{152}Eu source .sin file
- Use FT command to fit the data from the ^{152}Eu source .sin file.
- Use AD command to add data from the ^{56}Co source .sin file.
- Use the normalization factor to match the ^{56}Co data with the ^{152}Eu efficiency curve.
- use FT to fit the normalized combined data from the two sources.

The efficiency curve is obtained by using equation 4.2:

$$Efficiency = \exp\{[(A + Bx + Cx^2)^{-G} + (D + Ey + Fy^2)^{-G}]^{-1/G}\} \tag{4.2}$$

where A, B, C, D, E, F and G are the calibration parameters. A, B, and C describe the efficiency at low energies; similarly, D, E and F describe the efficiency at high energies and G is an interactions parameter between the high energy and the low energy regions and it determines the shape of the turnover between the two curves. x and y from equation 4.2 are given by:

$$x = \log(\frac{E_\gamma}{E1}) \tag{4.3}$$

$$y = \log(\frac{E_\gamma}{E2}) \tag{4.4}$$

where E1 and E2 have the values 100 keV and 1 MeV, respectively, and E_γ is the γ-ray energy [42].

An efficiency curve can be obtained by plotting the efficiency at various energies. This curve can then be used to determine the efficiency of the detector at energies different from those used to obtain the curve. For the analog system the data for efficiency calibration were only taken on the last weekend of the experiments since the two weekends were consecutive. For the digital system each weekend has a separate calibration because the measurements were performed 7 weeks apart. In total there are three calibration curves. Figures 4.3, 4.4 and 4.5 show relative efficiency curves obtained using ^{56}Co and ^{152}Eu sources for the different weekends.

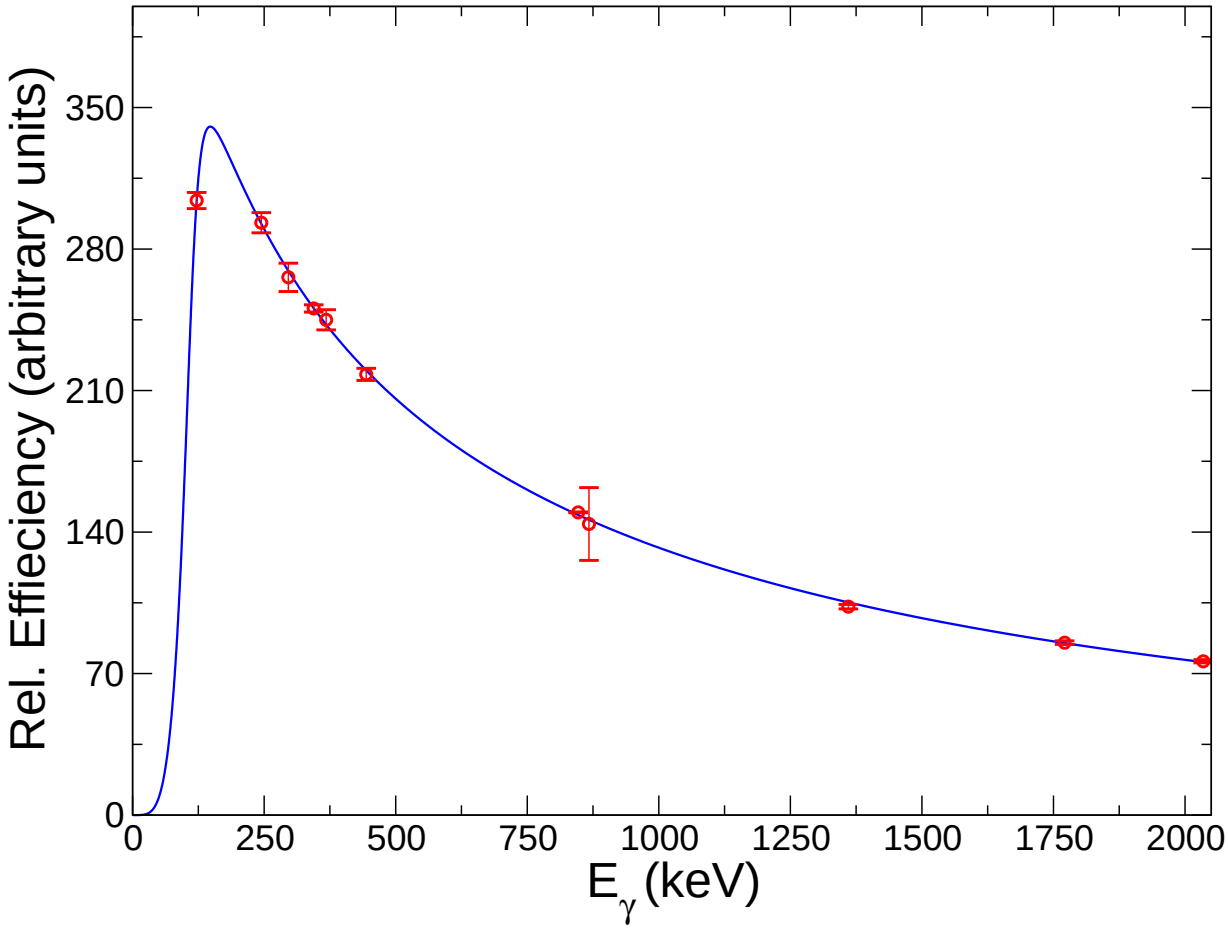

Figure 4.3: *Efficiency curve from* ^{56}Co *and* ^{152}Eu *sources obtained using analog system.*

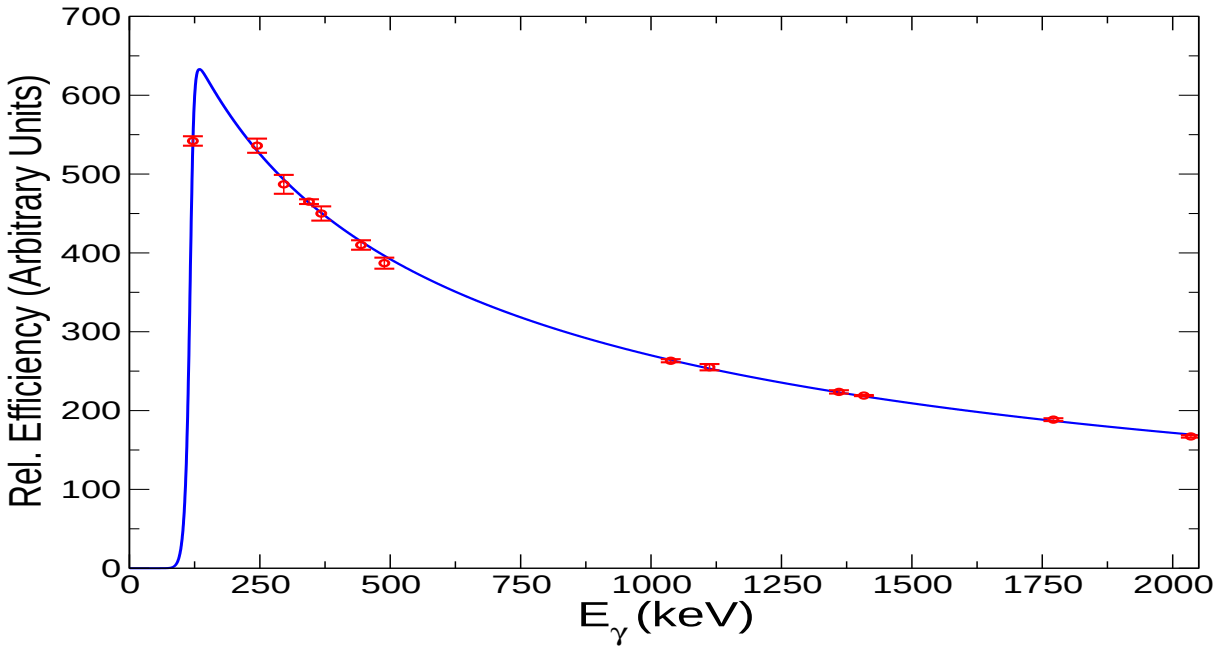

Figure 4.4: *Efficiency curve from* ^{56}Co *and* ^{152}Eu *sources obtained using the digital system - 1st weekend.*

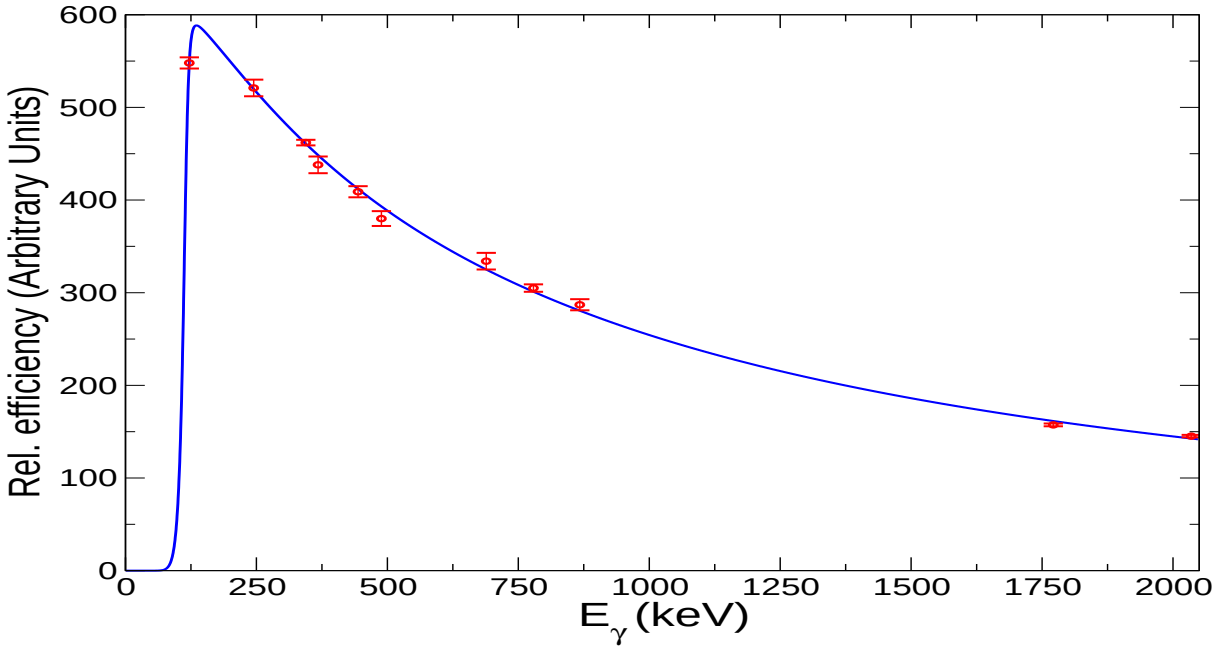

Figure 4.5: *Efficiency curve from* ^{56}Co *and* ^{152}Eu *sources obtained using the digital system - 2nd weekend.*

4.2.3 Intensity

The γ ray intensities are important in calculating the transition strength and the branching ratios. The intensity is calculated by dividing the area (in number of counts) by the efficiency which is obtained from the efficiency curve. The intensity of the γ ray, I_γ, can be calculated using equation 4.5.

$$I_\gamma = \frac{Area}{Efficiency} \tag{4.5}$$

The total intensity, I_T, is given by :

$$I_T = I_\gamma(1 + \alpha) \tag{4.6}$$

where α is the internal conversion coefficient and is given by:

$$\alpha = \frac{I_e}{I_\gamma} \tag{4.7}$$

The conversion coefficients used to calculate the intensities were taken from the BrIcc v2.35 page[1] [43]. In this work there were three efficiency curves from different experiments performed, therefore, three efficiency values were obtained for each γ ray. From the three efficiency values, three intensities were calculated. They were then averaged to one value of intensity for each γ ray. The calculated intensities for the γ rays of interest are presented in Section 4.3.5, together with the branching ratios.

[1] http://bricc.anu.edu.au

4.3 Results

4.3.1 Time Gate Condition

With the digital system the γ - γ coincidence rate reached a maximum frequency of about 50 kHz and a maximum counting rate (per clover) of 96 ks^{-1}. This means that more data were collected but there were also more randoms. In order to minimize the randoms in our data, the sorting code was edited and a time gate condition was set. Using the time spectrum, shown in Figure 4.6, the time gate was chosen to be from 1020 ns to 1030 ns.

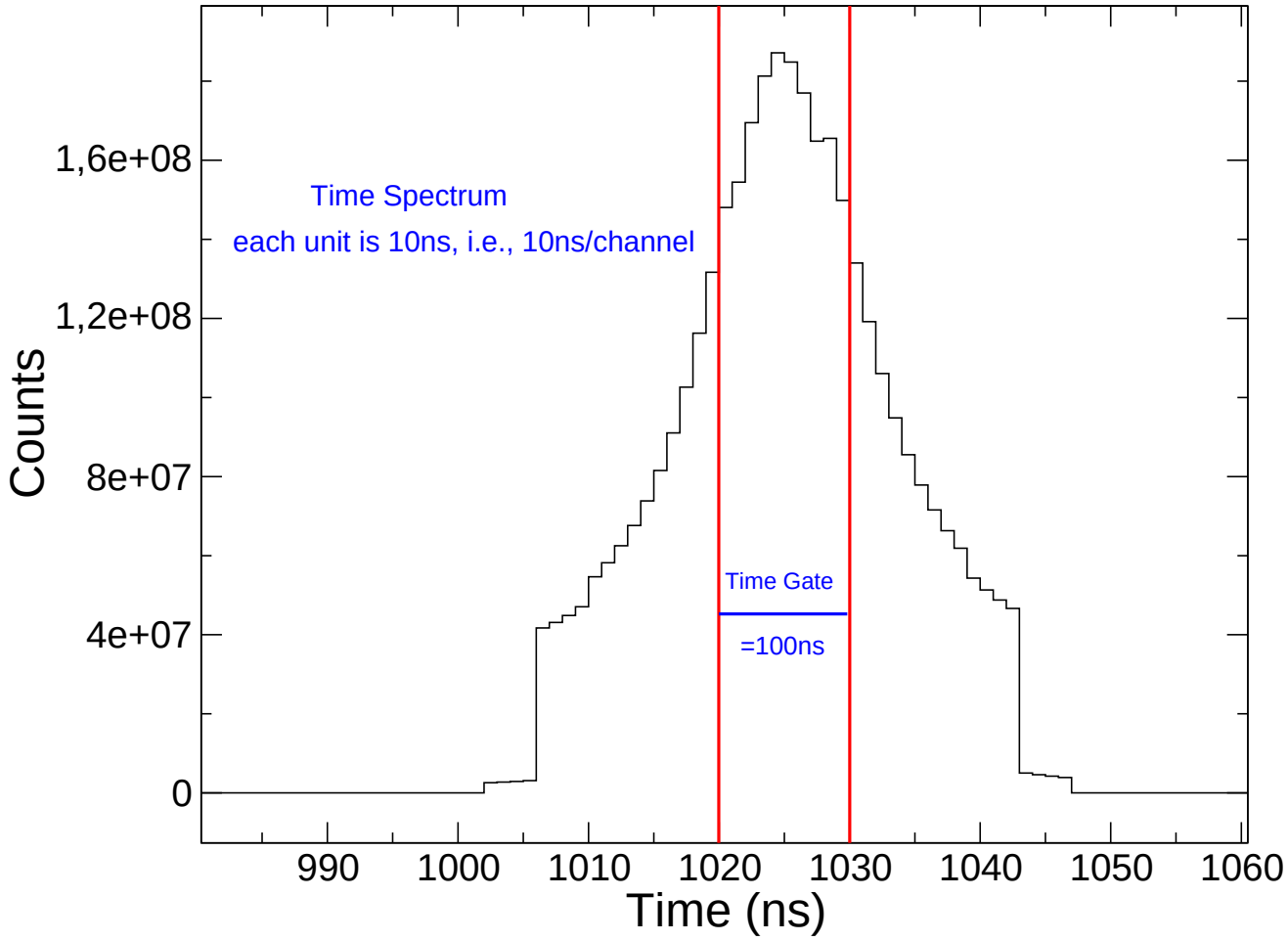

Figure 4.6: *Typical time spectrum, showing the time window gate used for sorting.*

The reason for setting the time-gate condition is to maximize the events from the nucleus of interest to be sorted,and the unwanted events, such as, randoms and background are

vetoed. A shorter time gate results in fewer randoms and the longer time gate results in more randoms. The random coincidences cannot be completely avoided but they can at least be minimized. Three sorts, each with a different time-gate, were performed; the first with 10 channels (100 ns), the second with 15 channels (150 ns), and lastly with 20 channels (200 ns). After sorting, the total projection spectra were obtained from the matrices. The total projection spectra obtained at different time gates are shown in Figure 4.7.

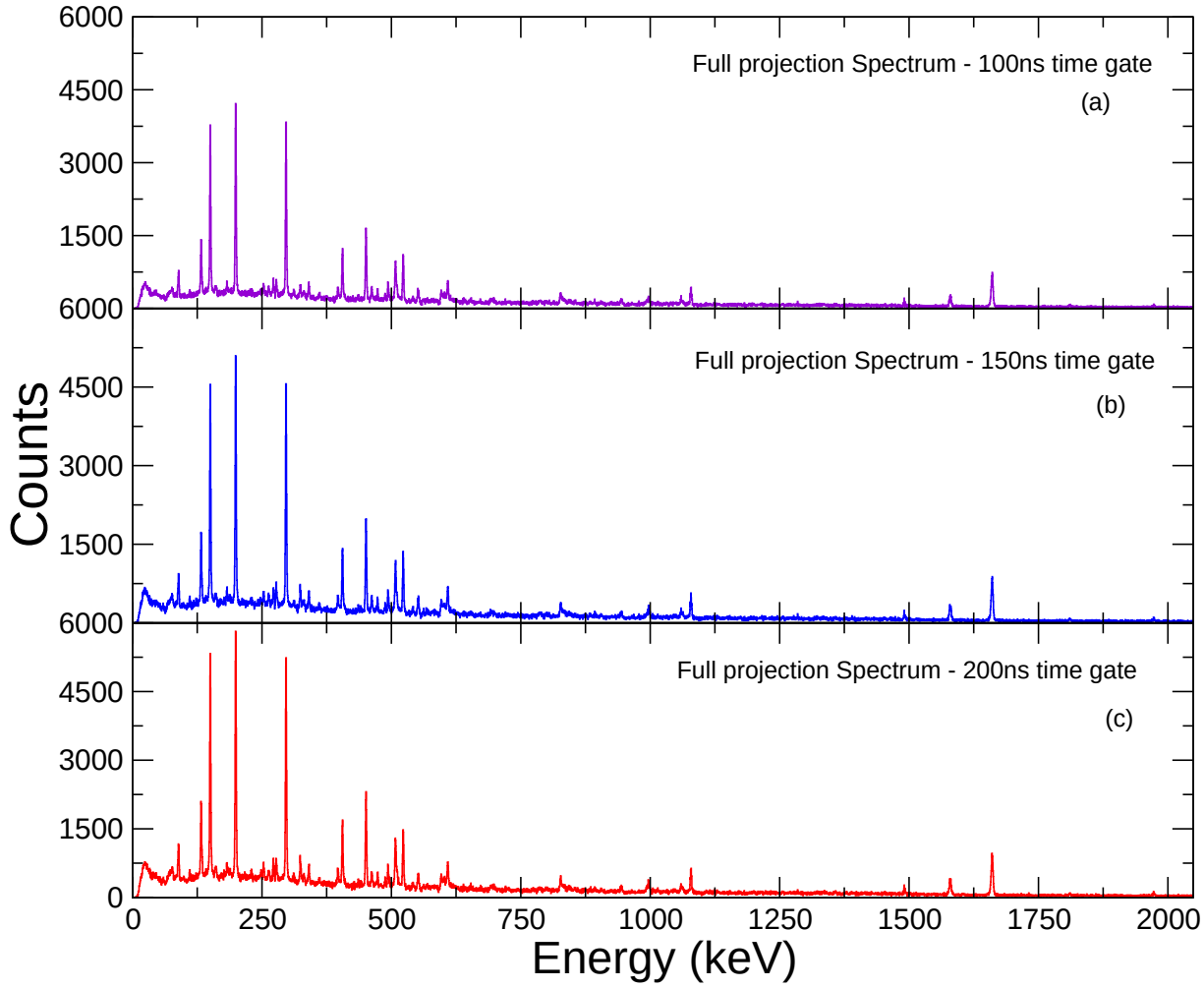

Figure 4.7: *Matrix projection spectra taken from matrices sorted with different time gate conditions.*

Figure 4.7 shows that spectrum sorted with 100 ns time gate has the least number of counts and the one sorted with 200 ns has the most. From the three total projection spectra, 1078 keV and 381 keV gates were set, and three 1078 keV gated spectra and three 381 keV gated spectra were obtained. From each gated spectrum the 1579 keV peak was fitted to obtain

the peak area. The background area, with the same number of channels as the peak area, was also obtained. In order to determine which time gate condition gives better ratio for each spectrum, the peak to background ratio (P/B) was calculated using equation 4.8.

$$P/B = \frac{PeakArea}{BackgroundArea} \tag{4.8}$$

4.3.2 Total projection and reaction products

As mentioned previously, four weekends of measurements were performed, two with the analog system and two with the digital system. Below the total projection spectra from all the performed experiments are shown. From the first two weekends, with the analog system, the collected data have 1.8 x 10^9 γ - γ coincidences in the total projection. Figure 4.8 shows the total projection spectrum for the analog system, i.e., the sum of the data obtained in weekend 1 and weekend 2. The ^{146}Gd γ -ray transitions observed with the prompt time condition are clearly marked.

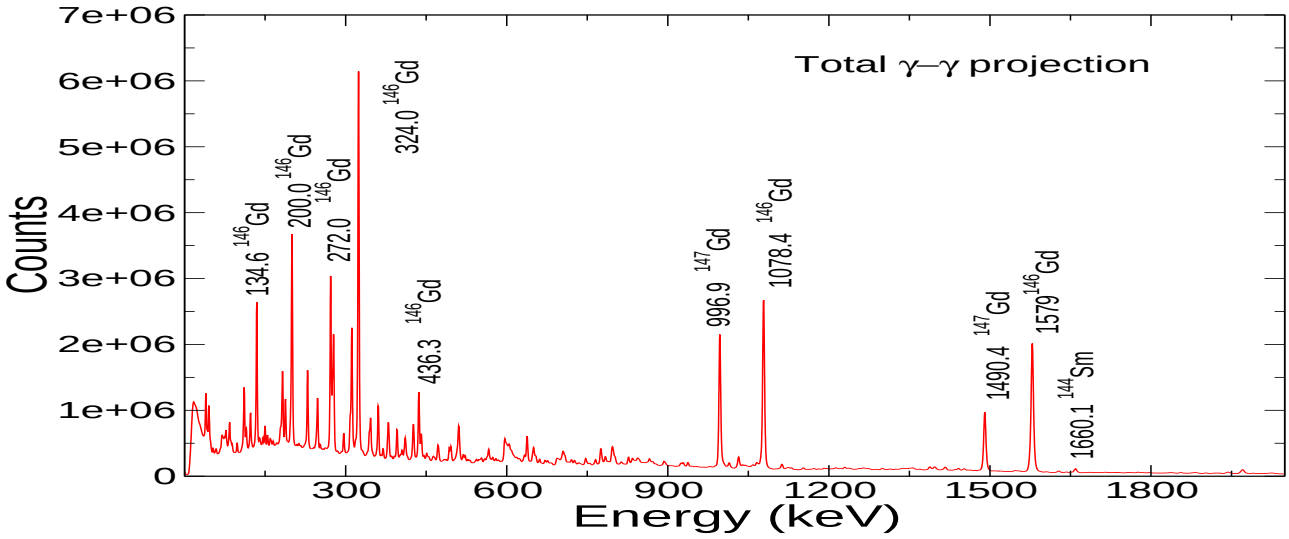

Figure 4.8: γ - γ *coincidence total projection with prompt time condition. Data were collected with the analog system.*

The total projection, with no time conditions, for both weekends of the digital have 8.5 x 10^9 γ - γ coincidences. With the time prompt condition of 100 ns, the first weekend had 5.6 x 10^8 events and the second weekend had 3.43 x 10^9, summing up to 3.99 x 10^9 γ - γ

coincidences. The total summed projection is shown in Figure 4.9 with the ^{146}Gd γ ray transitions observed in a prompt time condition clearly marked.

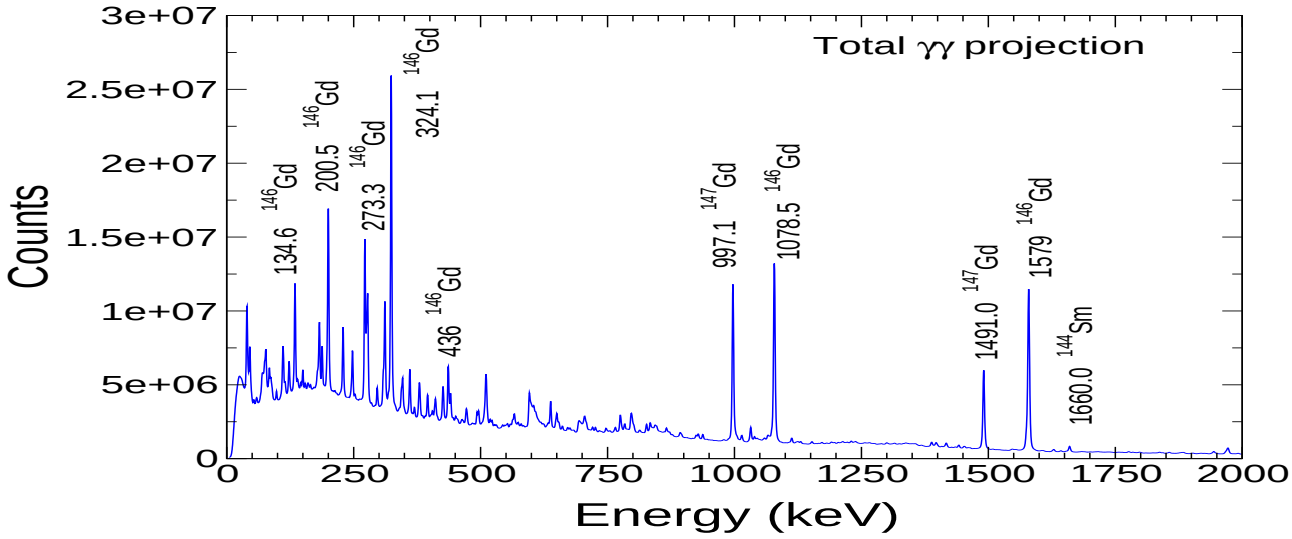

Figure 4.9: γ - γ *coincidence total projection with 100 ns prompt time condition. Data were collected with the digital system.*

The 85.91 % enriched ^{144}Sm target was used for all the experiments performed. The other 14.09 % was a composition of the other Sm isotopes, see Table 3.1 in Section 3.4.1. The reaction of interest was ^{144}Sm (α,2n)^{146}Gd, but there were other reactions that occurred and, therefore, other nuclei were produced. This was due to the fact that the target was not enriched to 100 % in ^{144}Sm. Other possible reactions are ^{147}Sm (α,2n)^{149}Gd, ^{148}Sm (α,2n)^{150}Gd, ^{149}Sm (α,2n)^{151}Gd, ^{150}Sm (α,2n)^{152}Gd, ^{152}Sm (α,2n)^{154}Gd, and ^{154}Sm (α,2n)^{156}Gd. There were also γ rays from the ^{144}Sm nucleus due to Coulomb excitation of the target. The known γ rays from the other nuclei were also marked in Figures 4.8 and 4.9. Furthermore, Figures 4.8 and 4.9 also compare data collected using different systems, namely, digital and analog system. From the Figures 4.8 and 4.9 it is clear that the digital system improved the data statistics by a factor of three.

4.3.3 iThemba LABS compared with Cologne experiment

This research was focused on re-investigating the 1905 keV transition from the $J^{\pi} = 6^{+}$ state to the $J^{\pi} = 3^{-}$ state which was observed by Caballero *et al.* [2] from the experiment performed at the University of Cologne. As mentioned earlier, the AFRODITE array had all of its clover detectors surrounded by the BGO shields whereas in Cologne not all of their Ge detectors had BGO shields and the array was nonsymmetric. It was, therefore, expected that the iThemba set up would give better results compared to the Cologne experiment. Figure 4.10 and Figure 4.11 compare the total projection spectra obtained from iThemba and Cologne measurements respectively. Although our data seem to have less background, the Cologne data seem to have better peak-to-background ratio at low energies, see Figures 4.12 and 4.13. The fact that the target used in our experiment was less enriched compared to the one used in the previous measurements might have contributed in improving the cross section resulting to better data quality in the Cologne experiment.

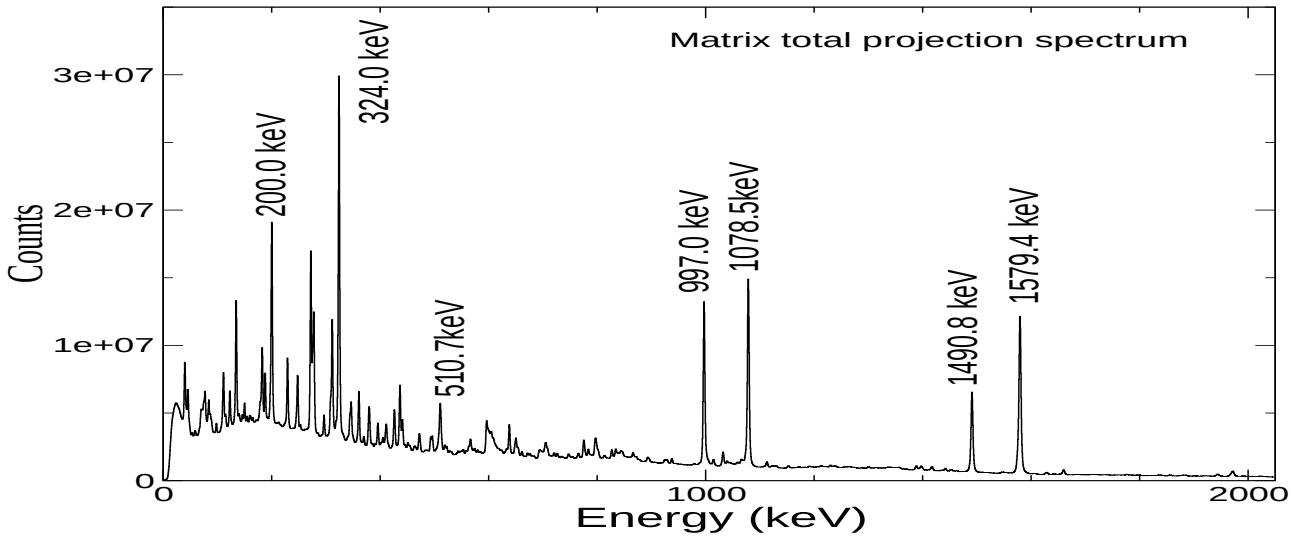

Figure 4.10: *Total projection spectrum from our data.*

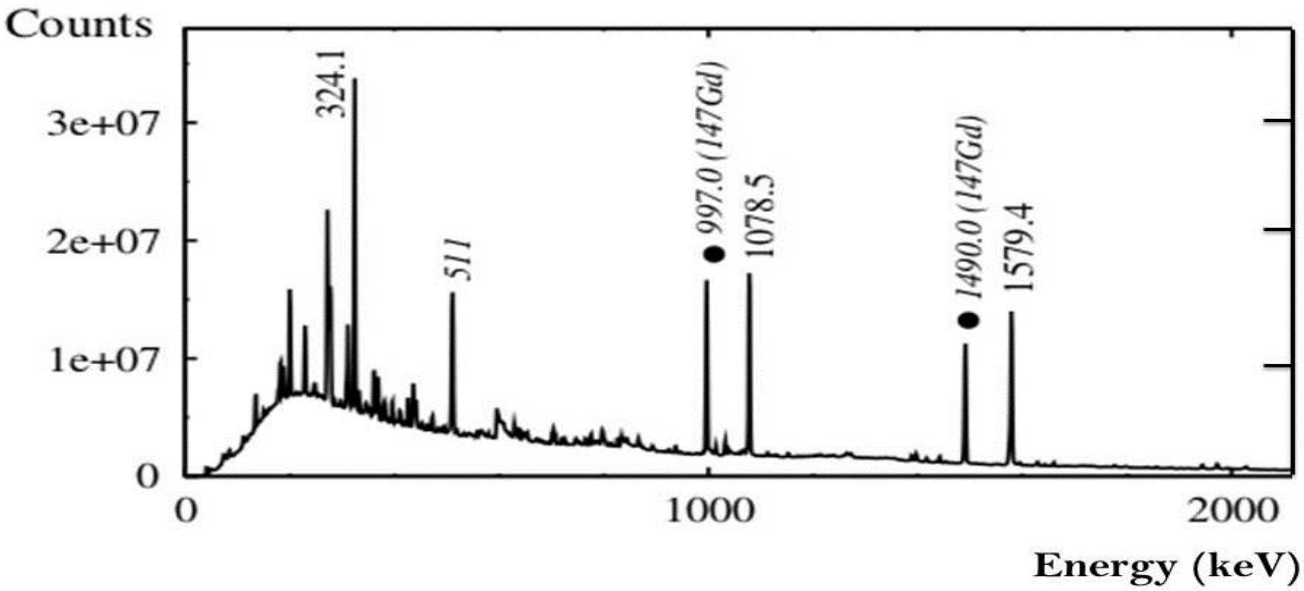

Figure 4.11: *Total projection spectrum from previous work [2].*

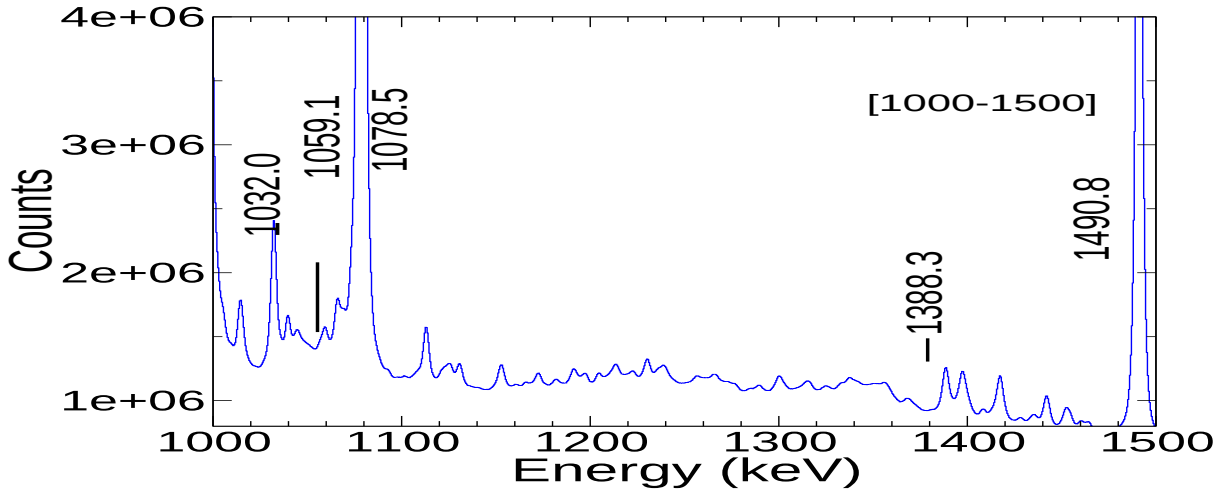

Figure 4.12: *Total projection [1000 - 1500 keV] from our data.*

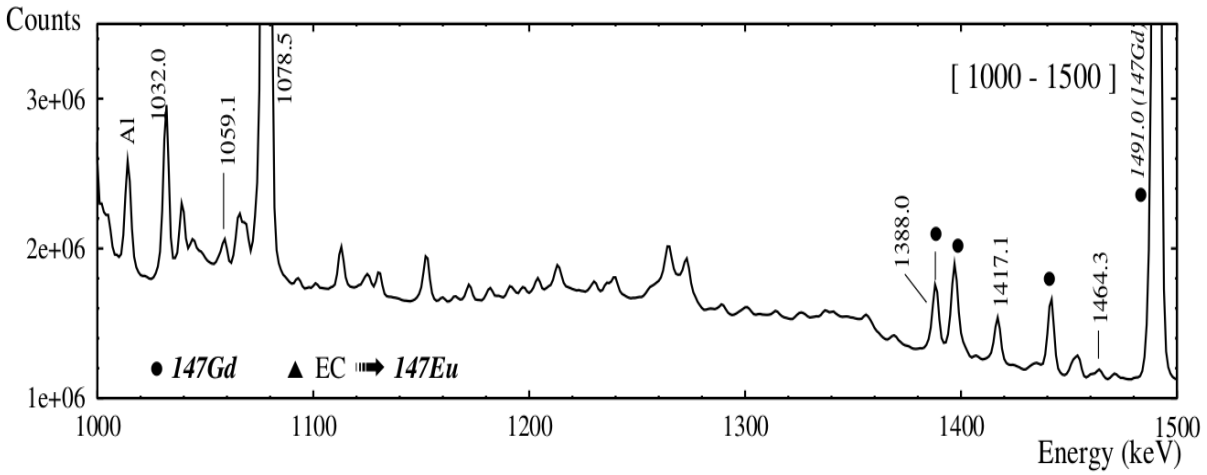

Figure 4.13: *Total projection spectrum expanded [1000 - 1500 keV], from previous work [2].*

Figure 4.12 is the expanded total projection from our work and Figure 4.13 shows the matrix pojection spectrum from the previous work. Indeed, the data from the previous work had fewer γ ray transitions from other nuclei than ^{146}Gd. Another important aspect which must be taken into consideration is the fact that the Cologne detection system have better resolution compared to that of iThemba, see Figures 4.12 and Figure 4.13.

4.3.4 382 keV Gate

After sorting the data, the E_γ-E_γ matrix was obtained and from this matrix a projection spectrum was obtained. From the matrix projection spectrum a gate was set on the 382 keV γ ray transition. The gate was placed using Slice from RadWare [42]. This was done to see transitions that are in coincidence with the 382 keV γ ray. From the 382 keV gated spectrum, shown in Figure 4.14, only the transitions in coincidence with the 382 keV γ ray should be seen. As shown in Figure 4.14, most of the transitions observed are from ^{146}Gd but there are other γ ray transitions from ^{156}Gd and ^{144}Sm. The observed ^{144}Sm γ ray transitions are a result of the ^{144}Sm target Coulomb excitation and transitions from ^{156}Gd are due to the ^{154}Sm (α,2n) reaction. One would not expect to see γ rays from these other nuclei (e.g. ^{156}Gd, ^{144}Sm, etc) since the gate was set on the ^{146}Gd 382 keV transition, but rather only ^{146}Gd γ ray transitions should be observed. On the one hand, ^{144}Sm has a 380.7 keV γ ray transition which is in coincidence with the 150.2 keV, 132.7 keV and the 1660.0 keV γ ray transitions. On the other hand, ^{156}Gd has a 380.4 keV transition which is in coincidence with the 551.3 keV, 507.7 keV, 451.0 keV, 296.3 keV, 1991.1 and the 88.6 keV γ ray transitions. It is therefore for this reason that when gating on a 382 keV γ ray peak, the above-mentioned transitions from ^{144}Sm and ^{156}Gd are also observed. ^{156}Gd 380.4 keV γ ray. Figure 4.15 presents the partial level scheme of ^{146}Gd and it clearly shows the transitions in coincidence with the 382 keV γ rays that are observed in the 382 keV gated spectrum. Figure 4.16 shows the partial level scheme of ^{144}Sm which has the transitions in coincidence with the ^{144}Sm 380.7 keV γ ray that are observed in the 382 keV gated spectrum. Figure 4.17 is the partial level scheme of ^{156}Gd showing the transitions in coincidence with the ^{156}Gd 380.4 keV γ ray transition that are observed in the 382 keV gated spectrum.

As suggested from previous work [2], when gating on the 382 keV γ ray (which in their case is 381 keV) the 1905 keV γ ray transition from the 6^+ state to the 3^- state should be observed, see Figure 4.18. Comparing the partial level schemes shown in Figures 4.15 and 4.18; the 502.7 keV and the 826.7 keV γ ray transitions de-exciting the 3484.1 keV energy level are observed, as expected, but the 1905 keV γ ray transition was not observed.

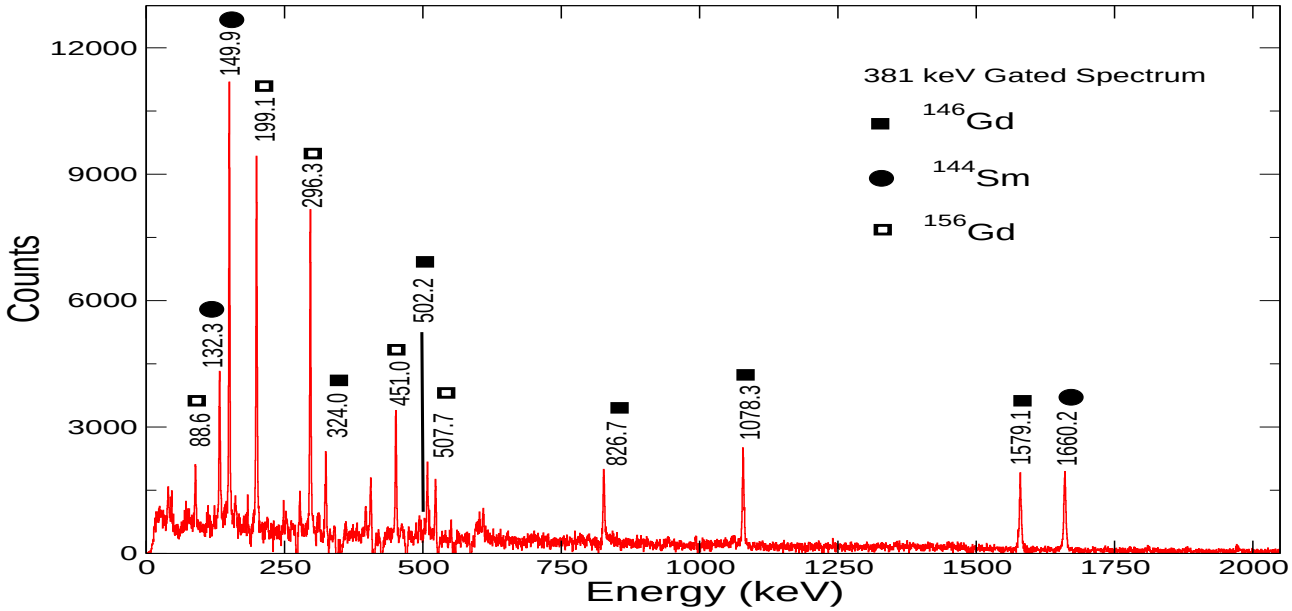

Figure 4.14: *Gamma ray transitions from the* ^{146}Gd*,* ^{144}Sm *and* ^{156}Gd *nuclei observed when gating on the 381 keV transition.*

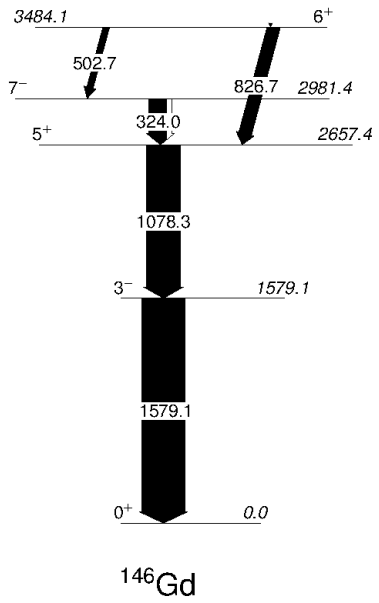

Figure 4.15: *Partial level scheme of* ^{146}Gd *showing the transitions in coincidence with the 382 keV* γ *ray.*

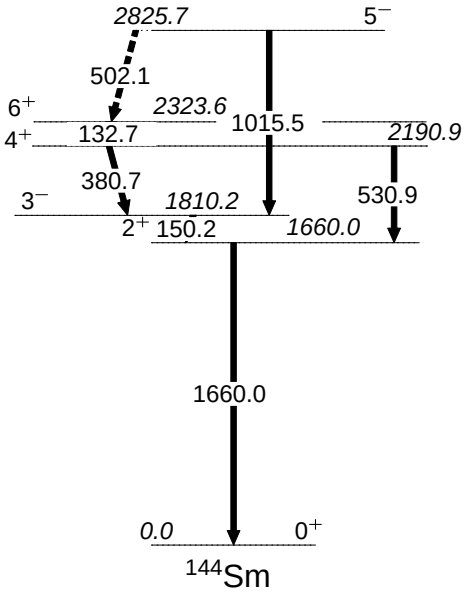

Figure 4.16: *Partial level scheme of* ^{144}Sm *showing the transitions observed in the 382 keV gated spectrum.*

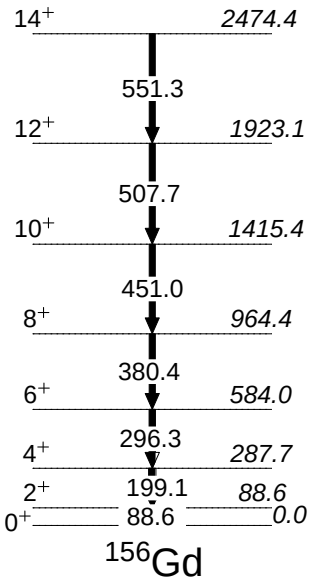

Figure 4.17: *Partial level scheme of* ^{156}Gd *showing the transitions observed in the 381 keV gated spectrum.*

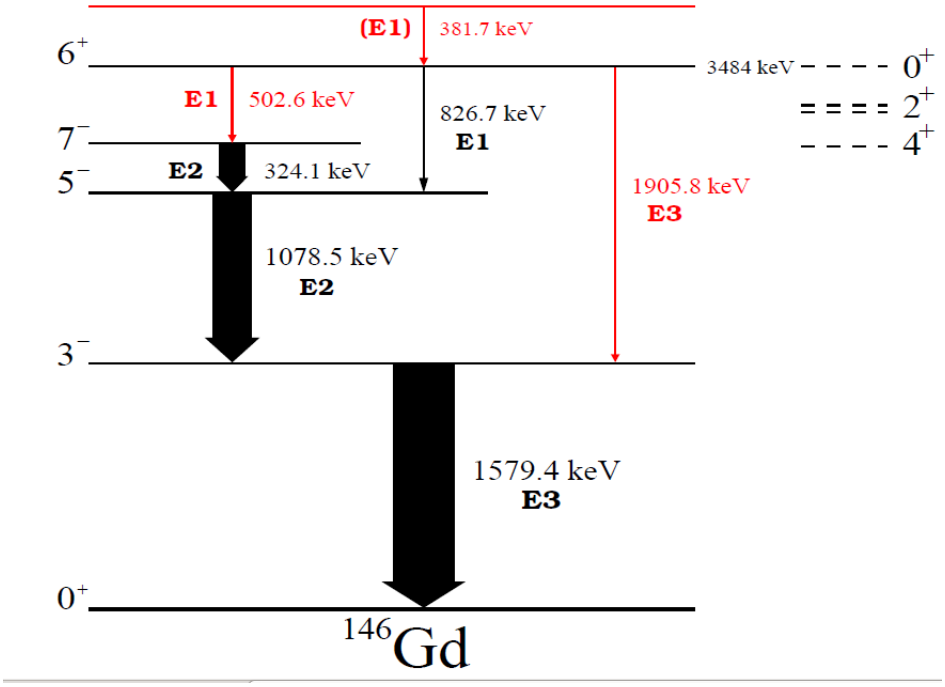

Figure 4.18: *A partial level scheme for ^{146}Gd showing transitions and levels related to the 3484 keV 6^+ state. Taken from previous work [2].*

Below the expanded 382 keV gated spectra is examined and it shows clearly the regions where the 502 keV, 826 keV and the 1905 keV γ ray transitions should be observed. Figure 4.19 shows the 826.7 keV peak taken from our work and Figure 4.20 shows the same 826.7 keV peak from previous work. The 826.7 keV γ ray transition of ^{146}Gd is much stronger in the data obtained from the previous measurement compared to our data, and is more enhanced and better resolved.

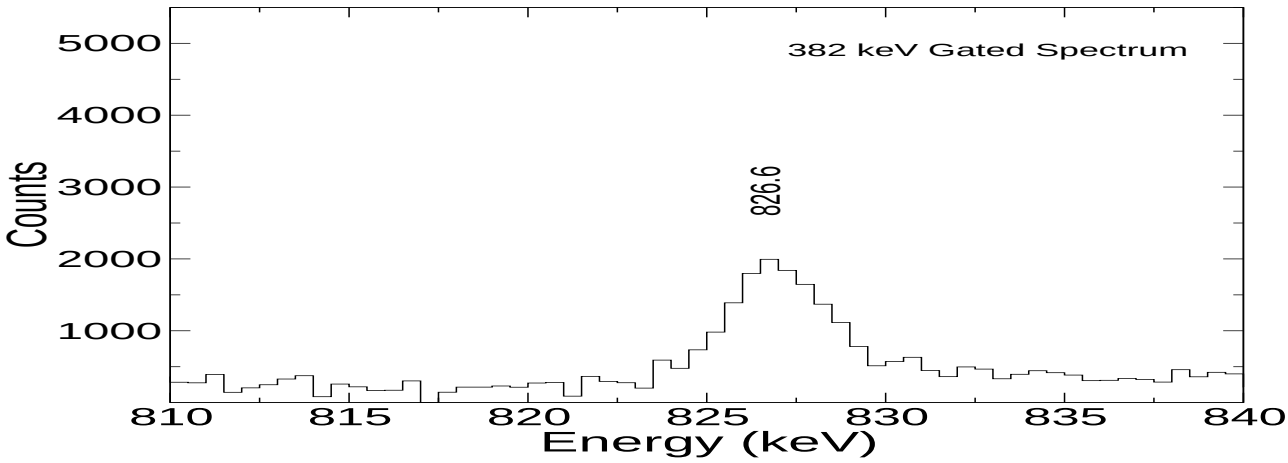

Figure 4.19: *The 826.7 keV γ ray peak observed in the 382keV gated spectrum in our work*

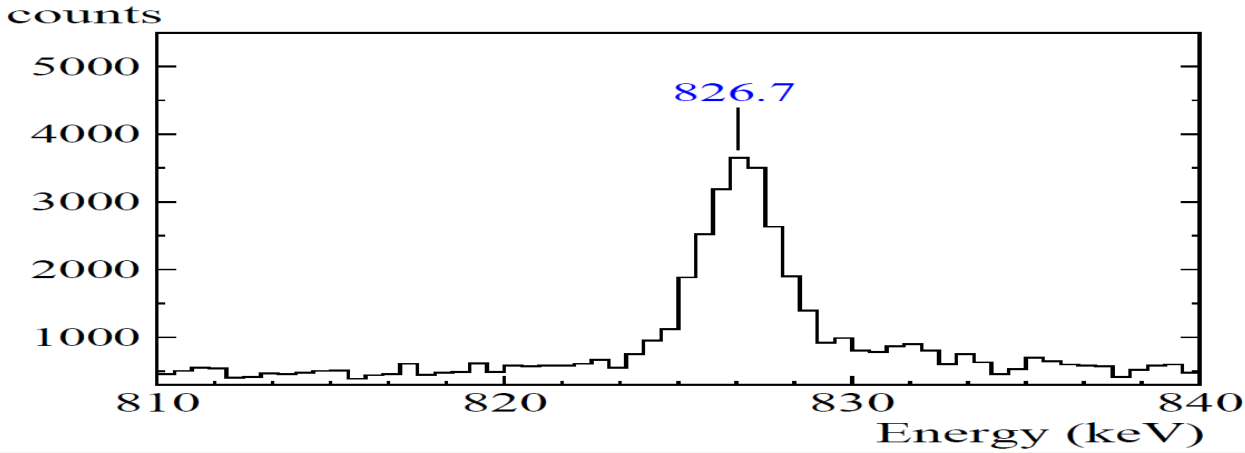

Figure 4.20: *The 826.7 keV peak as observed from the 381 keV gated spectrum. Taken from previous work [2].*

Figure 4.21 and Figure 4.22 further compare data from the present and the previous measurements. The 502 keV γ ray transition from ^{146}Gd was observed in both measurements. A 507 keV γ ray transition from ^{156}Gd was observed from our data. The ^{156}Gd evaporation residues were produced via the reaction ^{154}Sm(α, 2n) due to target impurities, see Table 3.1 in Section 3.4.1. Although the 511 keV peak observed in the previous measurement shows a bump on the left, see Figure 4.22, which might be an indication of the presence of the 507 keV γ ray transition, the production of the ^{156}Gd nucleus should be minimum since the target used is better enriched.

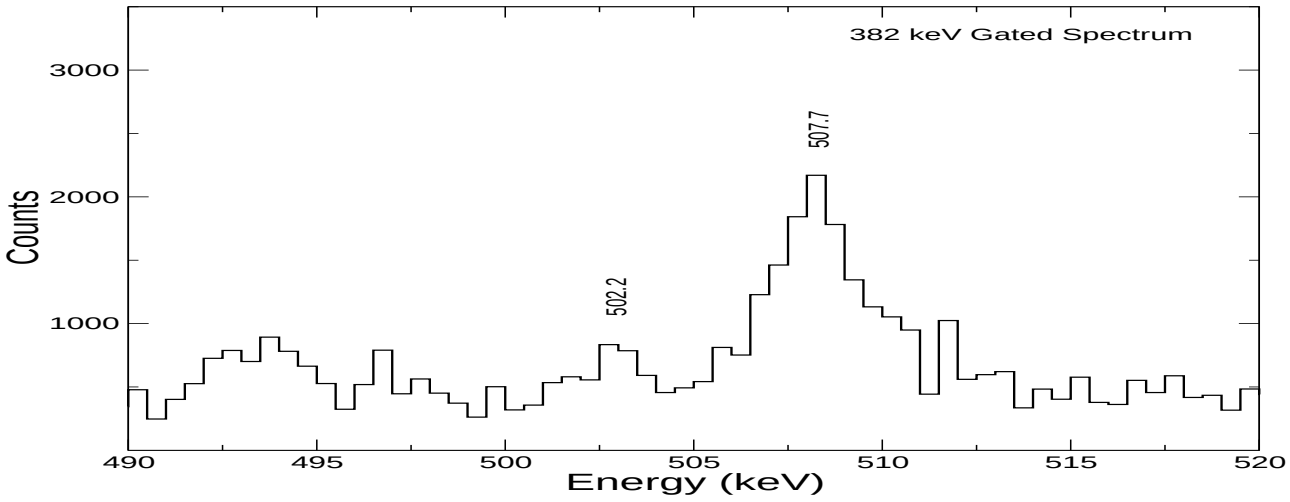

Figure 4.21: *502.2 from ^{146}Gd and the neighbouring 507.7 keV peak from ^{156}Gd as observed from the 382keV gated spectrum.*

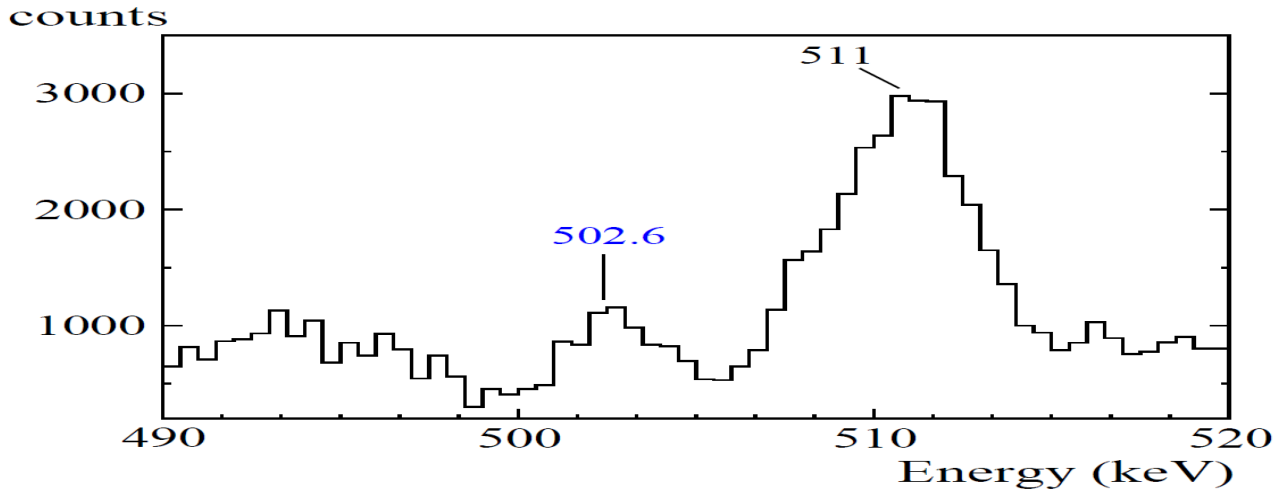

Figure 4.22: *502.6 keV peak as observed from the 381 keV gated spectrum. Taken from previous work [2].*

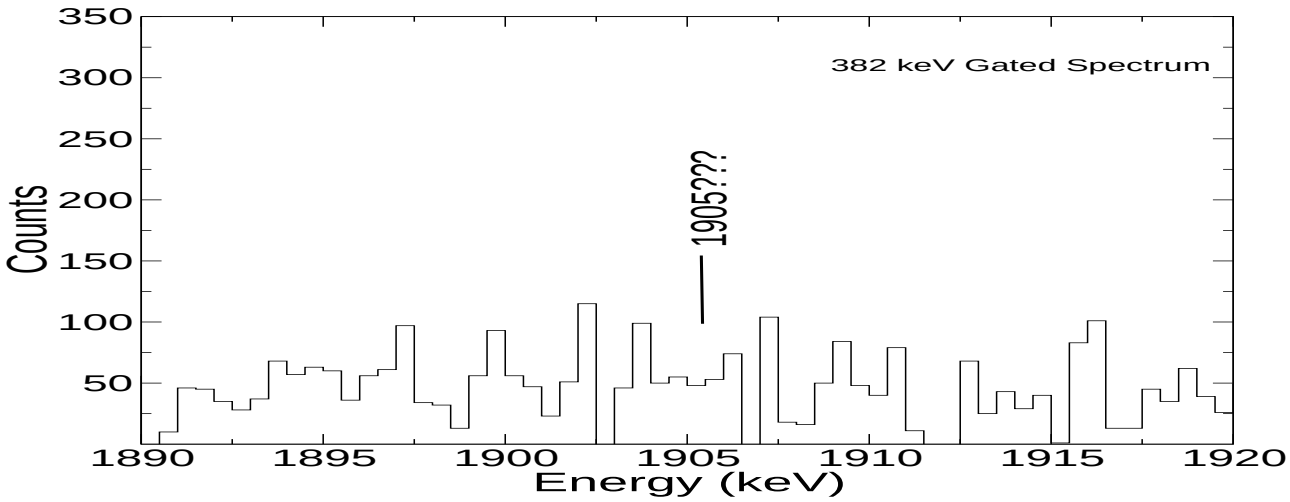

Figure 4.23: *The expanded 382 keV gated spectrum. It shows no evidence of the 1905 keV transition.*

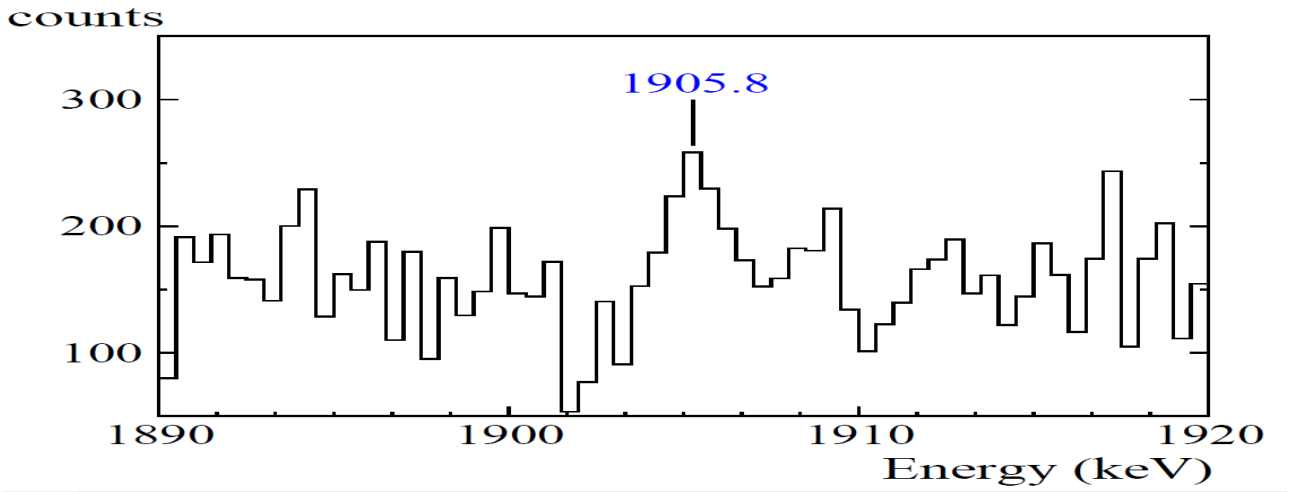

Figure 4.24: *1905.8 keV transition observed from the 381 keV gated spectrum taken from previous work [2].*

As mentioned previously, the presence of the 1905 keV γ ray transition from the 6^+ to 3^- will confirm the long standing prediction of two-phonon octupole vibrations in ^{146}Gd. The previous study only measured a very weak γ ray transition from ^{146}Gd decaying from 6^+ to 3^-, see Figure 4.18 and Figure 4.24. Figure 4.23 shows a spectrum obtained when gating on the 382 keV γ ray transition from our data and it shows no evidence of the presence of the 1905 keV γ ray which was observed in the previous study.

Noticeably, the 826 and the 502 keV peaks obtained from our data have less counts compared to the same peaks obtained from the previous work. It is therefore expected that the 1905 keV peak from our data be proportionally smaller than the one obtained from the previous work, given it exists. So to conclude whether the 1905 keV peak is present or not, branching ratios should be calculated and limits should be set on this extremely weak transition. The next section discusses the branching ratios and limit setting.

4.3.5 Branching Ratios And Limits

As mentioned in the previous section, in our 382 keV gated spectrum there was no evidence of the presence of the 1905 keV peak, nonetheless, an upper limit to its existence has been measured [44]. From the 382 keV gated spectrum, the 826 keV, 502 keV and the 1905 keV peaks were fitted and their areas/counts were obtained. Using the efficiencies from the respective efficiency curves, the intensities were calculated as discussed in Section 4.2.2. Tables 4.1, 4.2 and 4.3 show the calculated intensities of the 826 keV, 502 keV and 1905 keVγ ray transitions . In Tables 4.1, 4.2 and 4.3, A is the area of the peak, ΔA is the uncertainty of the area, eff is the efficiency, Δeff is the efficiency uncertainty, CC is the internal conversion coefficient, ΔCC is the internal conversion coefficient uncertainty, I_γ is the intensity and ΔI_γ is the intensity uncertainty. The intensity uncertainty was calculated using equation 4.9.

$$\Delta I_\gamma = \sqrt{(\frac{1}{eff})^2 \Delta A^2 + (\frac{1}{eff^2})^2 \Delta eff^2} \tag{4.9}$$

The total intensity for each gamma-ray was calculated by adding the three intensities. The intensities were then normalized, as illustrated Table 4.4.

Table. 4.1. *The intensities of the 826, 502 and 1905 keV γ ray transitions from the analog system data*

E_γ (keV)	A	ΔA	eff	Δeff	CC	ΔCC	I_γ	Δ I_γ
826	6059	127	148.13	1.48	0.001639	0.000023	41.0	1.0
502	1268	95	202.7	2.03	0.00467	0.00007	6.3	0.5
1905	$\leq$130		79.10	0.79	0.001560	0.000022	$\leq$1.6	

μs

Table. 4.2. *The intensities of the 826, 502 and 1905 keV γ ray transitions from the digital system, first weekend.*

E_γ (keV)	A	ΔA	eff	Δeff	CC	ΔCC	I_γ	Δ I_γ
826	8086	1263	300.6	3.006	0.001639	0.000023	26.9	4.2
502	2459	151	388.7	3.88	0.00467	0.00007	6.3	0.4
1905	$\leq$175		178	1.78	0.001560	0.00022	$\leq$ 1.0	

Table. 4.3. *The intensities of the 826, 502 and 1905 keV γ ray transitions from the digital system, second weekend.*

E_γ (keV)	A	ΔA	eff	Δeff	CC	ΔCC	I_γ	Δ I_γ
826	8086	1262	296.6	2.97	0.0001639	0.000023	27.3	5.3
502	1451	181	393.3	3.94	0.00467	0.00007	3.7	0.5
1905	$\leq$276		157	1.57	0.00156	0.00022	$\leq$ 1.8	

Table. 4.4. *Normalized intensities for the 502, 826 and the 1905 keV γ ray transitions.*

E_γ (keV)	I_γ (Analog)	I_γ (Digital W1)	I_γ (Digital W2)	I_γ (Total)	I_γ (Normalized)
826	40.9(1)	26.9(5)	27.3(42)	95.1(45)	100(3)
502	6.3(5)	6.3(5)	3.7(5)	16.3(17)	17(3)
1905	$\leq$1.6	$\leq$1.0	$\leq$1.8	$\leq$4.4	$\leq$5

Table 4.5 shows the normalized intensities for the 502, 826 and the 1905 keV γ rays [3].

Table. 4.5. *Normalized intensities for the 502, 826 and the 1905 keV γ ray transitions from previous work [3].*

E_γ (keV)	I_γ	I_γ (Normalized)
826.7	2.05(14)	100
502.6	0.32 (4)	15.6
1905.8	0.13(6)	6.3

Calculating the ratio between the 826 keV and 502 keV γ ray transitions :

$$I_{ratio(iTL)} = \frac{I(826)}{I(502)} = \frac{100}{17.1} = 5.8(6)$$

$$I_{ratio(Col)} = \frac{I(826)}{I(502)} = \frac{100}{15.6} = 6.4(5)$$

In the above calculations, $I_{ratio(iTL)}$ is the intensity ratio obtained from our data and $I_{ratio(Col)}$ is the intensity ratio from previous work [3]. Clearly the experimental ratios are in agreement. From these measurements, the limit for the 1905 keV γ ray transitions was set to the intensity of $\leq$6. Using gf3, the peak 1905 keV was fitted and the obtained area was used to determine the intensity and the intensity obtained was $<$5.

Chapter 5

Discussion And Conclusion

The aim of this work was to re-investigate the existence of the 1905 keV E3 γ ray transition from the 6^+ at 3483.1 keV to the 3^- in ^{146}Gd as reported in the previous study. The goal was to characterize the two-phonon octupole 6^+ state, a member of the two-phonon octupole quartet, as proposed from previous work [2]. This study was to identify whether the ^{146}Gd nucleus exhibits the two-phonon octupole vibrations or not. In this work, the ^{144}Sm(α, 2n) fusion evaporation reaction was used. The ^{144}Sm target, enriched to 85.91 %, of 3.0 mg/cm^2 thickness was bombarded with beam of α particles at an energy of 26.3 MeV. The experiment was performed at iThemba LABS using the AFRODITE array which had 8 clover detectors that were surrounded by BGO shields for Compton suppression. Four clover detectors were placed at 90° and the other four at 135°. The collected data were analyzed with the RadWare software package [42].

The 382 keV coincidence gate was set from the E_γ-E_γ matrix projection spectrum to confirm whether the previously observed 1905 keV γ ray was present or not. From this work the 502 keV and the 826 keV γ ray transitions, both de-exciting from the 3484.1 keV energy level, were observed as expected, but the anticipated 1905 keV γ ray transition, which was expected to also de-excite the 3483.1 keV level, was not observed. From the present work there is no evidence of the 1905 keV E3 transition and, therefore, no evidence of the two-phonon octupole vibrations in ^{146}Gd.

Nevertheless, adequate data statistics and a more efficient gamma ray detection system could possibly be important in confirming the 1905 keV γ ray from the 6^+ state to the

3^- state and characterizing the the other two-phonon octupole quartet members (0^+, 2^+ and 4^+). With the proposed GAMKA array at iThemba LABS this can be achieved. The GAMKA array will have 16 clover detectors, 7 more clover detectors than the AFRODITE array used in this work, all surrounded by the BGO shields. The GAMKA array, together with the digital system, will provide enhanced γ ray data acquisition capabilities.

Bibliography

[1] P. Kleinheinz *et al.*, Phys. Rev. Lett. **48**, 1457 (1982)

[2] L. Caballero, PhD thesis, Universidad de Valencia, (2005)

[3] L. Caballero *et al.,* Phys. Rev. C **81**, 031301(R) (2010)

[4] A. Bohr and B. R. Mottelson, *Nuclear Structure Vol. 2* , World Scientific Singapore, (1998).

[5] A. Bohr and B. R. Mottelson and M. Fys. and M. Dan, Vid. Selsk. **27**, (1953)

[6] K.S. Krane, *Introductory Nuclear Physics*, John Wiley & Sons. Inc., (1988)

[7] H. Jansen, Nature **435**, 207, (2005)

[8] M. Massimi, *Pauli's Exclusion Principle*, Cambridge University Pres, (2005)

[9] S.M. Wong, *Introductory Nuclear Physics*, Wiley-VCH Verlag GmbH & Co. KGaA, (2004)

[10] M. Thoennessen, Rep. Prog. Phys. **76**, 056301, (2013)

[11] Shell Model of Nucleus - HyperPhysics, (2013)

[12] T.D. Singo, AIMS Essay, (2006)

[13] R.F Casten, *Nuclear Structure from a Simple Perspective*, Oxford Science Publication, (2000)

[14] K.L. Green, M.Sc thesis, University of Guelph

[15] W. Nazarewicz, P. Olanders, I. Ragnasson, J. Dudek, G.a Leander, P. Möller and E. Ruchowska, Nucl. Phys. A **429**, 269 (1984)

[16] D.J. Rowe and J.L Wood, *Fundamentals of nuclear models*, Word Scientific, (2010)

[17] P.E. Garrett and J.L. Wood, Journal Of Physics G: Nuclear and Particle Physics, (2010)

[18] http://www.physics.uoguelph.ca/ pgarrett/Kpi.jpg, (2013)

[19] S.N.T. Majola, M.Sc thesis, University of Cape Town, (2011)

[20] P. A. Pipidis, PhD thesis, Florida State University, (2006)

[21] G. Nelson and D. Reilly, Gamma-ray interactions with matter, (2013)

[22] S. DeBenedetti, *Nuclear Interactions*, John Wiley and Sons, Inc., New York, London, (1964)

[23] P. Regan, Post Graduate Nuclear Experimental Techniques (4NET) Course Notes, University of Surrey, (2003)

[24] R. Bock, *Heavy Ion Collisions, Volume 2*, North Holland Publishing Company, (1980)

[25] N. Bohr, Nature **137**, 344, (1936)

[26] N.Y. Kheswa *et al.*, Nucl. Instr.and Meth. in Phys. Res. A **613**, 389-391, (2010)

[27] N.Y. Kheswa *et al.*, Nucl. Instr.and Meth. in Phys. Res. A **590**, 114, (2008)

[28] R. T. Newman *et al.*, proceeding of Balkan School on Nucl. Phy., September 1-10, 1998, Istanbul-turkey, Balkan Physics letters, 82, (1998)

[29] D. Hawcroft, slides presented at XXXIII Zakopane School of Physics, Poland, (1998)

[30] S.S Ntshangase, PhD thesis, University of Cape Town, (2011)

[31] T. Szucs *et al.*, Eur.Phys.J. A **44**, 513-519, (2010)

[32] R.M. Lieder, Experimental Techniques in Nuclear Physics, ed. D.N Poenaru and W. Greiner, Walter de Gruyter, (1997)

[33] P.M. Jones *et al.*, Nucl. Instr. and Meth. in Phy. Res. A **362**, 556, (1995)

[34] T.E. Madiba, M.Sc thesis, University of the Western Cape, (2008)

[35] G. Duchêne *et al.*, Nucl. Instr. and Meth. in Phys. Res. A **432** , 90, (1999)

[36] J.L. Conradie, PhD thesis, University of Stellenbosch, (1992)

[37] S.W. Yates *et al.*, Z Phys. A - Atoms and Nuclei **324**, 417-432, (1986)

[38] S.W. Yates *et al.*, Phys. Rev. C **36**, 2143, (1987)

[39] W.R. Leo, *Techniques for Nuclear and Particle Physics Experiments*, Springer, (1994)

[40] P. Jones, Digital Data Aqcuisition System, http://daq.tlabs.ac.za/experiments/ddas-1/expert-guide, (2013)

[41] XIA LLC, User's Manual Digital Gamma Finder (DGF) Pixie-4, (2009)

[42] D. C. Radford, Nucl. Instrum. Methods Phys. Res. A **361**, 297 (1995), URL: http://radware.phy.ornl.gov

[43] Australian National University - Department of Nuclear Physics, (2013), URL: http://bricc.anu.edu.au/

[44] L.A Curie, Anal. Chem. **40**, 586, (1968)